sustainability

MDPI

Article

# Multi-Feature Coordinated Adaptive ECMS with Fuzzy Logic for Low-Carbon Sustainable Fuel Cell Hybrid Electric Commercial Vehicles

**Xuening Zhang , Xiaodong Liu *, Juan Du, Xiaorui Li and Xintian Jiang**

School of Mechanical & Automotive Engineering, Liaocheng University, Liaocheng 252000, China; 2420230210@stu.lcu.edu.cn (X.Z.); dujuan02@lcu.edu.cn (J.D.); 2520230207@stu.lcu.edu.cn (X.L.); 2520230204@stu.lcu.edu.cn (X.J.)

* Correspondence: liuxd@lcu.edu.cn; Tel.: +86-635-8239970

**Abstract**

This paper introduces a multi-feature coordinated adaptive equivalent consumption minimization strategy (MFCA-ECMS) using fuzzy logic control (FLC) to enhance hydrogen efficiency in fuel cell hybrid electric commercial vehicles (FCHECVs) and extend the lifespan of the fuel cell system (FCS), contributing to sustainable, low-carbon transport. First, a baseline ECMS model is established for the FCHECV, whilst the optimal equivalent factor (EF) is determined using a multi-island genetic algorithm (MIGA) based on representative driving cycles. Second, an adaptive EF framework is developed to overcome the inherent limitation of conventional ECMS—its reliance on a fixed EF—by dynamically integrating three operational features: variation in the battery's state of charge (SOC), the rate of change in the FCS's output power, and fluctuations in vehicle power demand. Third, feature-specific adaptive weights are assigned and updated in real time using a fuzzy inference system to regulate the EF online, incorporating multiple features. Simulations are conducted under different initial SOC levels (90% and 45%) across different driving cycles. The results demonstrate that the MFCA-ECMS consistently reduces hydrogen consumption (HC). Compared to the charge-depleting and charge-sustaining (CD-CS) strategy, it achieves HC reductions of 17.98% on the stochastic driving cycle (Random-C) and 18.73% on the urban dynamometer driving schedule (UDDS), outperforming both CD-CS and conventional ECMS in all tested scenarios. Furthermore, the MFCA-ECMS actively suppresses FCS power fluctuations. Regardless of the initial SOC, the proportion of power change rates within the reasonable range exceeds 97%, thereby contributing to extending the FCS lifespan. This reduces emissions and operating costs, enabling sustainable hydrogen-powered commercial vehicle deployment.

**Keywords:** multi-feature coordinated; equivalent consumption minimization strategy; fuzzy logic control; fuel cell hybrid electric commercial vehicles; low-carbon; sustainable

Check for updates

Academic Editors: Longxing Wu, Zhiqiang Lyu, Renjing Gao and Muyao Wu

Received: 3 May 2026
Revised: 19 June 2026
Accepted: 23 June 2026
Published: 2 July 2026

**Copyright:** © 2026 by the authors. Licensee MDPI, Basel, Switzerland. This article is an open access article distributed under the terms and conditions of the Creative Commons Attribution (CC BY) license.

## 1. Introduction

The international community has committed to limiting global warming to a maximum of 2 °C above pre-industrial levels, a goal that necessitates significant decarbonization of the fossil-fuel industry [1,2]. The transportation sector—particularly heavy-duty commercial vehicles, which emit substantially higher levels of carbon dioxide than passenger cars—is under increasing pressure to reduce its emissions [3]. Fuel cell hybrid electric commercial vehicles (FCHECVs) offer distinct advantages over battery electric vehicles (BEVs) in terms of energy efficiency and driving range, especially under heavy loads [4]. However, integrating fuel cells with batteries requires effective energy management strategies (EMSs) to optimize power flow and minimize HC. Hence, advancing EMS research is critical for the successful deployment of zero-emission FCHECVs [5,6].

Recent EMS technologies fall into three methodological categories: rule-based, optimization-based, and learning-based approaches [7]. Among these, rule-based strategies are characterized by straightforward logic, high operational efficiency, and ease of implementation, which has led to their widespread adoption [8]. These methods typically rely on established rules derived from engine external characteristic curves. Within this framework, the drive motor actively manages torque to keep engine operation predominantly within its high-efficiency range, thereby enhancing powertrain efficiency and fuel economy under specific driving conditions [9]. In the context of fuel cell electric vehicles (FCEVs), rule-based multi-objective optimization EMSs have been shown to significantly reduce real-time HC while concurrently extending fuel cell durability [10]. Furthermore, another critical advantage of rule-based methods lies in their ability to precisely extract and apply fuel cell output power rules, ensuring real-time responsiveness and effective EMS optimization [11]. Among these approaches, fuzzy logic control (FLC) stands out for its operational reliability and strong interpretability, making it particularly suitable for real-time implementation [12]. By leveraging predefined rule bases and membership functions (MFs), FLC enables smooth parameter adaptation and maintains robust performance under uncertain, time-varying operating conditions [13]. Recently, research has increasingly focused on enhancing FLC performance through evolutionary optimization techniques.

Despite their widespread use, rule-based EMSs often lack rigorous mathematical analysis and rely heavily on practitioner expertise, which may not guarantee optimal control [14]. To address this limitation, researchers are increasingly turning to optimization-based methodologies, broadly classified into global and real-time optimization techniques [15]. Among global optimization methods, dynamic programming (DP) is frequently used to enhance power distribution in hybrid power systems [16]. By applying Bellman's optimality principle, DP decomposes the optimization problem into a series of time-step subproblems, defines a stage cost function for each, and solves them recursively, yielding the optimal control sequence for time-domain optimization [17]. In addition, Pontryagin's minimum principle (PMP) provides an alternative global optimization approach, enabling a suitable power distribution that meets real-time optimization requirements [18]. Specifically, PMP is applied to dynamic multi-power-source systems by minimizing the Hamiltonian function at each time increment [19]. Furthermore, integrating PMP with collaborative optimization algorithms enables simultaneous resolution of speed-planning and energy-management challenges in FCEVs [20]. While both DP and PMP can derive globally optimal solutions, they come with significant computational burdens due to the need for discrete state and input spaces and interpolation calculations [21]. As a result, DP and PMP primarily serve as benchmark models for evaluating the theoretical performance limits of alternative EMSs in research and development contexts [22].

In light of the practical limitations of global optimization techniques, real-time optimization-based EMSs have been developed, notably model predictive control (MPC) and the equivalent consumption minimization strategy (ECMS) [23,24]. Current MPC research focuses on addressing increasingly complex, multi-objective, and coupled control challenges, with three principal advancements: The first involves integrating fuel cell degradation models to jointly optimize energy efficiency and stack durability [25]. The second incorporates connected-vehicle data—such as upcoming speed profiles and road grades—to enable coordinated optimization across energy management, velocity planning, and air supply control [26,27]. The third adopts hierarchical MPC architectures, where distinct control layers operating at different temporal resolutions reconcile global optimality with computational tractability and real-time feasibility [28]. Recent advancements have established MPC as a powerful control framework; however, its effectiveness remains contingent on the availability of accurate predictive models. Moreover, the demands of online optimization create an inherent trade-off between prediction horizon length and computational efficiency, posing significant challenges for real-time applications, particularly in embedded vehicle control systems.

In contrast, ECMS operates on an instantaneous optimization principle that relies on the equivalence between hybrid power sources. In FCEVs, the conventional ECMS uses a fixed EF to allocate power in real time. This simplification limits adaptability under changing driving conditions, especially during transient events. To overcome this limitation, adaptive ECMS (A-ECMS) dynamically tunes the EF in real time, enhancing overall energy efficiency across various operational scenarios [29]. A-ECMS methodologies are broadly classified based on their adaptation mechanisms. One common approach is SOC-feedback-based adaptation, where the deviation between the battery's SOC and its reference trajectory serves as the primary feedback signal, with the EF adjusted in real time using proportional-integral (PI) control or fuzzy inference methods [30]. Alternatively, preview-based adaptation leverages short-term predictions of vehicle speed, road slope, and other drivetrain-relevant variables to co-optimize the EF sequence over a moving prediction window [31]. Furthermore, driving-condition-classification-based adaptation identifies the current driving pattern—such as urban, highway, or hill-climbing—in real time and retrieves the corresponding precomputed EF map derived from offline global optimization [32]. Despite significant research on ECMS-based methods, notable limitations remain. The EF selection is sensitive, and optimal values vary with driving conditions. Moreover, current adaptive mechanisms are mostly heuristic, relying on empirically tuned rules that lack predictive power. As a result, these methods may struggle with optimality and robustness in dynamic or unforeseen scenarios.

Driven by advancements in artificial intelligence, learning-based energy management systems (EMSs) have emerged as a rapidly evolving field, particularly those based on reinforcement learning (RL) and its variants, such as deep Q-learning (DQL), double deep Q-networks (DDQN), and deep deterministic policy gradient (DDPG) [33,34]. Unlike static or model-dependent methods, RL-based EMSs learn optimal control policies through iterative interactions between the agent and the environment, enabling adaptive decision-making under uncertainty. Empirical applications demonstrate their effectiveness across various operational contexts. For example, DQL has been used to coordinate speed planning and power distribution for fuel cell electric buses operating in signalized arterial corridors, resulting in measurable reductions in HC [35]. Similarly, DDQN dynamically adjusts EMS parameters based on short-term velocity forecasts, improving fuel economy across diverse urban and highway driving cycles [36]. Furthermore, DDPG enables co-optimization of vehicle-level energy use and microgrid operational costs in integrated vehicle–grid-infrastructure systems, thereby promoting overall energy efficiency [37]. Collectively, these approaches improve robustness, adaptability, and real-time responsiveness, which are essential qualities for implementing EMSs in dynamic, real-world transportation settings. However, despite these advancements, the practical deployment of learning-based methods remains limited by their heavy reliance on extensive, high-quality training datasets. Gathering such data can be time-consuming and computationally expensive, and the resulting policies may not generalize well to unseen operating conditions.

Building on the preceding analyses, rule-based, optimization-based, and learning-based EMSs each offer distinct advantages but also suffer from inherent limitations, including suboptimal control, high computational demands, and a heavy reliance on extensive training data. In this context, integrating FLC with ECMS—specifically, the dynamic online adaptation of EFs through fuzzy inference—has emerged as a pivotal research direction in the development of A-ECMS. For instance, an adaptive neuro-fuzzy inference system (ANFIS) has been employed to optimize the reference SOC trajectory, thereby accommodating diverse driving scenarios [38]. In parallel, FLC has been combined with a driving-condition classification mechanism to enable real-time adjustment of EF [39]. Furthermore, to better utilize macroscopic traffic information, a backpropagation (BP) neural network has been implemented for long-term energy planning, while an FLC performs online fine-tuning of ECMS parameters [40]. Collectively, these approaches leverage the interpretability and nonlinear reasoning capabilities of fuzzy inference, allowing the ECMS to adapt its decision-making based on either real-time measurements or short-term forecasts. This adaptability ultimately leads to improved fuel economy under uncertain operating conditions. Moreover, fuel cells inevitably degrade over long-term operation due to electrode material degradation, catalyst loss, membrane damage, and fluctuations in operating conditions [41]. This reduces efficiency and output power while increasing maintenance costs. An effective EMS should therefore mitigate factors that accelerate degradation—especially frequent power fluctuations.

Despite recent advances, current fuzzy-logic-based A-ECMSs face three significant limitations: First, they tend to rely heavily on a single state variable—most commonly the battery's SOC deviation—when adapting EFs. This narrow focus neglects the intertwined effects of the FCS power dynamics and the vehicle's transient power demands on optimal energy allocation. Second, there is no systematic rule-design framework that explicitly considers the synergistic interactions among multiple characteristic variables. As a result, it becomes challenging to simultaneously optimize power-tracking accuracy, FCS operational stability, and the fidelity of transient responses across different driving conditions. Third, the literature lacks a multi-feature collaborative A-ECMS specifically designed for FCHECVs. In this regard, the concurrent objectives of energy efficiency, durability preservation, and drivability assurance have not been adequately addressed. Therefore, this paper introduces an online adaptive framework called the MFCA-ECMS. This framework enables real-time calculation of the EF by integrating three key measurable features: the deviation of the battery's SOC from its reference trajectory, the rate of change in FCS output power, and temporal variations in vehicle power demand. A multi-input fuzzy inference system dynamically adjusts the adaptive weights for each feature, enabling continuous, closed-loop regulation of the EF. Consequently, optimal energy management performance is maintained throughout vehicle operation.

The remainder of this paper is organized as follows: Section 2 presents the modeling of the FCHECV powertrain system. Section 3 details the design and formulation of the MFCA-ECMS. Section 4 provides a comprehensive simulation and validation of the proposed strategy across various driving cycles. Finally, Section 5 concludes the paper with key findings, limitations, and suggestions for future work.

## 2. FCHECV Modeling

This study examines a plug-in FCHECV, as illustrated in Figure 1. Its powertrain includes three key components—a traction motor, an automated manual transmission (AMT), and a final drive—all integrated into a single driveline. The AMT and final drive together function as a gear-reduction and torque-multiplication unit, ensuring adequate traction during acceleration and sufficient braking torque during deceleration. The vehicle features a dual-source hybrid power architecture that combines a proton-exchange membrane FCS with a lithium-ion battery pack. The FCS output voltage is regulated via a bidirectional DC/DC converter and then combined with the battery's output. This combined power is delivered to the motor controller as needed. Under low-load conditions, either source can meet the demand; during high power demands, both sources work together. Additionally, the battery pack supports plug-in charging from the external grid, enhancing flexibility in replenishing energy and improving the overall system efficiency [42].

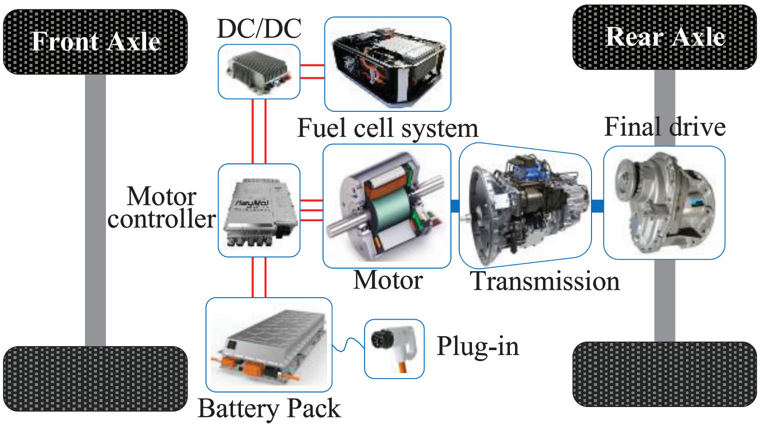


**Figure 1.** Powertrain architecture of the FCHECV [42].

### 2.1. Vehicle Dynamics

In energy management modeling, a simplification based on longitudinal dynamics is used to represent the vehicle system. This analysis explicitly excludes considerations of stability, ride comfort, and passenger comfort. As a result, the vehicle is modeled as a rigid point mass, meaning that factors such as axle load transfer, suspension compliance, and structural deformation are not accounted for. Assuming that the longitudinal forces are balanced, the tractive force delivered to the wheels must equal the total driving resistance. This total driving resistance includes rolling resistance, aerodynamic drag, grade resistance, and inertia resistance (acceleration). Given standard driving condition inputs—such as vehicle speed, road gradient, and the demand for longitudinal acceleration—the longitudinal force balance equation is formulated as Equation (1):

$$F_{req} = mgf \cdot \cos\alpha + \frac{1}{2}C_d \cdot \rho_a \cdot A_f \cdot u^2 + mg \cdot \sin\alpha + \delta m \cdot \frac{du}{dt} \tag{1}$$

where the variables $m$, $g$, and $f$ denote the vehicle's mass, gravitational acceleration, and rolling resistance coefficient, respectively, while the variable $\alpha$ represents the road slope angle. At the same time, $C_d$, $\rho_a$, and $A_f$ indicate the air resistance coefficient, air density, and vehicle frontal area, respectively. The variable $u$ represents the vehicle's speed, and $\delta$ is the rotational mass correction coefficient; $du/dt$ represents the vehicle's acceleration. The specific powertrain parameters of the FCHECV under investigation are provided in Appendix A. Subsequently, the required power ($P_{req}$) of the vehicle can be calculated using Equation (2):

$$P_{req} = F_{req} \cdot u \tag{2}$$

Currently, the vehicle's power demand is primarily met by both the battery power supply and the FCS. Thus, the power demand must also satisfy Equation (3):

$$P_{req} = P_{fc} + P_{bat} \tag{3}$$

### 2.2. FCS Model

The FCS is the primary power source for the FCEV, delivering the necessary propulsion power. The proton-exchange membrane fuel cell (PEMFC) is preferred due to its high power density, efficient low-temperature operation, and rapid load response. Therefore, this study uses a PEMFC-based FCS with a peak power output of 123.18 kW as the traction source for the FCHECV. The FCS model used here is a quasi-static efficiency map derived from experimental data that links net output power to HC. This method is common in ECMS-based energy management, treating the fuel cell as an energy source rather than a detailed electrochemical system [14,29]. While effective for this scope, it does not account for nonlinear voltage effects due to polarization. Future work will develop a full voltage mechanism model for higher fidelity [43]. The hydrogen mass flow rate is calculated during quasi-steady-state operation using Equation (4):

$$\dot{m}_{H_2} = \frac{P_{fc}}{\eta_{fc}(P_{fc}) \cdot LHV} \tag{4}$$

In this context, $\dot{m}_{H_2}$ represents the HC rate, $P_{fc}$ indicates the output power of the FCS, and $\eta_{fc}$ refers to the FCS's efficiency. It is important to note that $\eta_{fc}$ is dependent on $P_{fc}$, and its specific value can be determined through bench tests. Additionally, $LHV$ stands for the lower heating value of hydrogen, which is a constant at 120,000 J/g. The relationships among the output power, efficiency, and HC rate of the FCS are illustrated in Figure 2.

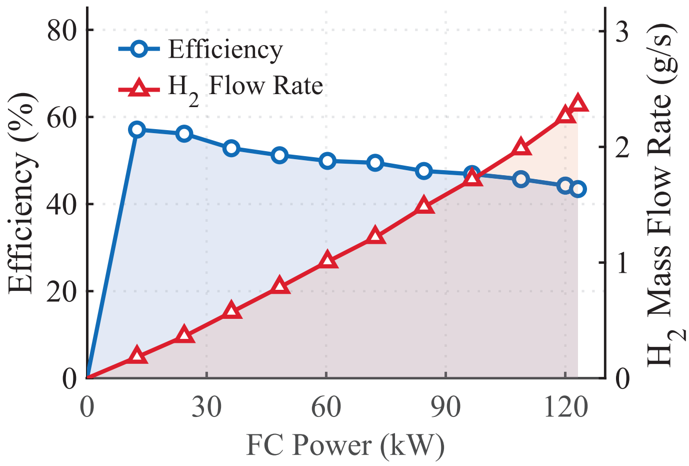


**Figure 2.** Performance map for FCS.

It is essential to emphasize that $\eta_{fc}$ exhibits a nonlinear dependence on its net output power $P_{fc}$. Specifically, $\eta_{fc}$ increases with rising $P_{fc}$ up to a distinct peak—corresponding to the system's optimal operating point—beyond which further power augmentation results in diminishing efficiency. This behavior defines an efficiency-optimal power band for the FCS. Consequently, the EMS for the studied FCHECV must prioritize operation within this high-efficiency band to minimize hydrogen mass consumption and maximize energy economy.

### *2.3. Battery Model*

The studied FCHECV employs lithium–iron phosphate battery packs as its secondary energy storage. The nominal system voltage is 530 V, and the rated capacity is 100 A·h. For modeling purposes, this study adopts the Rint equivalent circuit model, parameterized using experimental charge/discharge data under representative operating conditions. This model balances structural simplicity with sufficient fidelity to capture key battery behaviors, including open-circuit voltage hysteresis, SOC-dependent internal resistance, and dynamic voltage response, as illustrated in Figure 3.

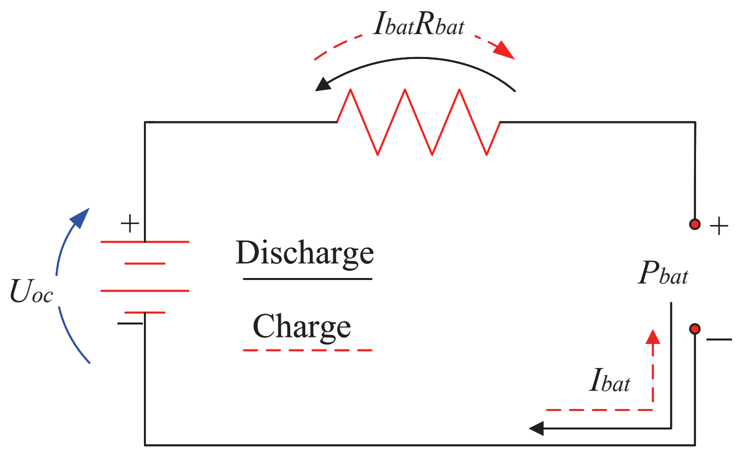


**Figure 3.** Rint equivalent circuit model.

The battery pack current $I_{bat}$ is derived from the instantaneous power–voltage relationship, as expressed in Equation (5):

$$I_{bat} = \frac{U_{oc} - \sqrt{U_{oc}^2 - 4R_{bat}P_{bat}}}{2R_{bat}} \tag{5}$$

The battery pack current is $I_{bat}$, $U_{oc}$ represents the open-circuit voltage, and $P_{bat}$ indicates the battery's output power. The $I_{bat}$ sign is significant: a positive $I_{bat}$ indicates that the battery is discharging, while a negative $I_{bat}$ indicates that it is charging. Key dynamic parameters—specifically, $U_{oc}$ and the SOC-dependent internal resistance ($R_{bat}$)—show considerable distinction between charging and discharging. These parameters have been identified experimentally as strongly nonlinear functions of the SOC, based on extensive bench testing conducted at normal temperature and given C-rate conditions, as shown in Figure 4.

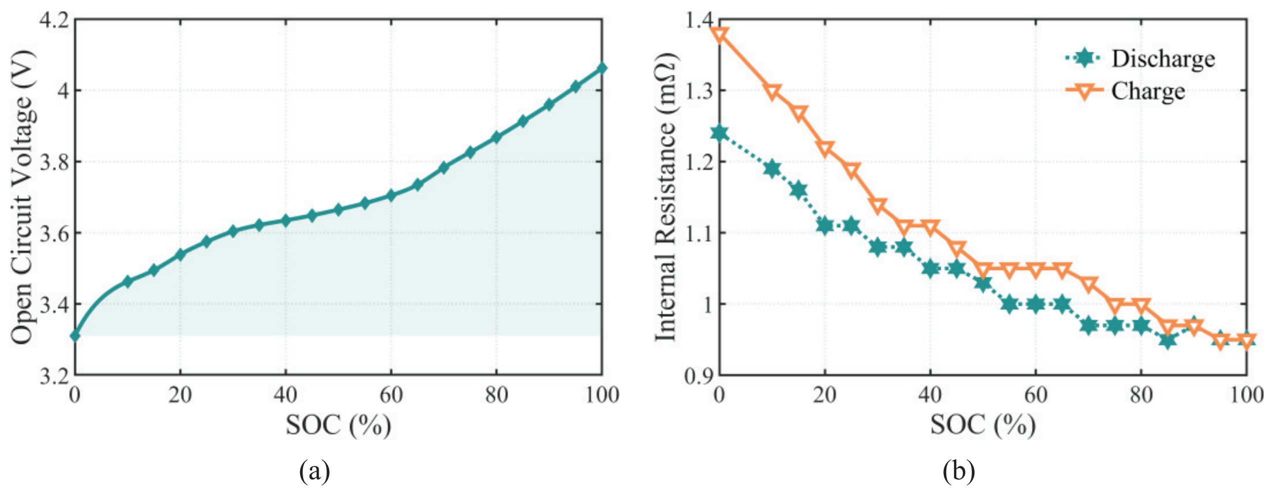


**Figure 4.** Battery characteristics: (**a**) open-circuit voltage; (**b**) resistance.

Accurate SOC estimation is essential for improving battery model reliability and predictive accuracy. This study uses the ampere-hour integration method for SOC estimation due to its widespread real-world application and proven short-term accuracy. The SOC at time $t_f$ is given by Equation (6):

$$SOC(t_f) = SOC(t_0) - \frac{1}{Q_{bat}} \int_{t_0}^{t_f} I_{bat}(t)\, dt \tag{6}$$

Here, $SOC(t_f)$ and $SOC(t_0)$ denote the battery's SOC at the final and initial time points, respectively; $Q_{bat}$ represents the battery's rated capacity; and $t_0$ and $t_f$ denote the initial and final time instants, respectively. Therefore, the change in the battery's SOC (ΔSOC) is described by Equation (7):

$$\Delta\mathrm{SOC} = \mathrm{SOC}(t_f) - \mathrm{SOC}(t_0) = -\frac{1}{Q_{bat}}\int_{t_0}^{t_f} I_{bat}(t)\,dt \tag{7}$$

### 2.4. AMT Model

The FCHECV features a six-speed AMT as a key powertrain component. This configuration combines the high mechanical efficiency of traditional manual transmissions with the convenience of electronic actuation. The multi-gear ratio modulation offers three main advantages: it allows a smaller motor to deliver higher torque at lower speeds, maintaining the vehicle load capacity; it keeps both the motor and fuel cell operating within their most efficient ranges; and it reduces driver workload while enhancing hydrogen efficiency and extending the powertrain components' lifespan. The transmission model is given by Equation (8):

$$\begin{cases} T_{AMT\_out} = T_{AMT\_in} \cdot i_g \cdot \eta_{AMT} \\ n_{AMT\_out} = n_{AMT\_in} / i_g \end{cases} \tag{8}$$

where $T_{AMT\_out}$ and $T_{AMT\_in}$ refer to the output and input torque of the AMT, respectively, while $n_{AMT\_out}$ and $n_{AMT\_in}$ denote the AMT's output and input rotational speeds, respectively. The variable $i_g$ represents the speed ratio of the AMT, while $\eta_{AMT}$ denotes the efficiency of the AMT across various speed ratios.

### 2.5. Motor Model

The FCHECV is equipped with a 350 kW, 2200 N·m permanent-magnet synchronous motor (PMSM) that can operate in both directions, serving as a traction motor and a regenerative brake generator. This dual-function design allows a more compact chassis, reduces the overall vehicle weight, and maintains high energy conversion efficiency across the entire speed–torque range. Consequently, the onboard FCS requires less hydrogen, extending the driving range and improving the transient power response. For energy management, a static PMSM model including both motoring and generating modes is used, as given by Equation (9):

$$P_m = \begin{cases} \dfrac{T_m \cdot n_m}{9550} \cdot \dfrac{1}{\eta_m} & (T_m \geq 0) \\ \dfrac{T_m \cdot n_m}{9550} \cdot \eta_m & (T_m < 0) \end{cases} \tag{9}$$

where $P_m$ represents motor power, $T_m$ indicates motor torque, $n_m$ signifies the motor's rated rotational speed, and $\eta_m$ denotes motor efficiency, which is a function of both $T_m$ and $n_m$, as specified in Equation (10):

$$\eta_m = f(n_m, T_m) \tag{10}$$

This functional relationship has been experimentally characterized through dynamometer testing, as shown in Figure 5.

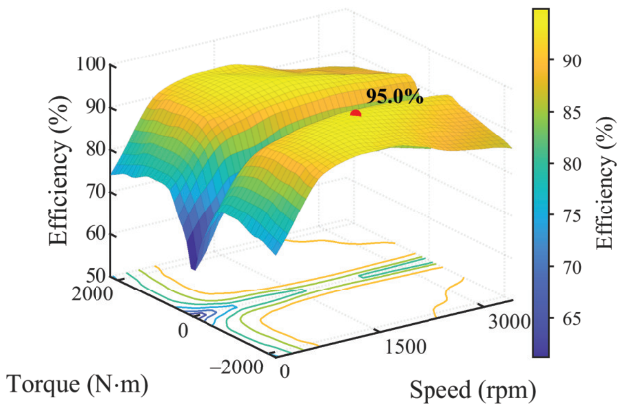


**Figure 5.** Motor efficiency.

## 3. Formulation of MFCA-ECMS

In real-time ECMS applications, the EF determines how power demand is distributed between the hybrid power sources. Conventional ECMS implementations rely on static, predetermined EFs that do not adapt well to changing or diverse operating conditions. Furthermore, they fail to adequately account for the FCS's nonlinear characteristics, particularly in terms of energy efficiency and transient response. To overcome these limitations, this study introduces an MFCA-ECMS. The proposed method embeds a baseline EF—derived from offline optimization based on representative driving cycles—within an online adaptive framework. Within this framework, an adaptive EF adjustment law is developed using three key state variables: the deviation in battery SOC, the instantaneous FCS output power, and the rate of change in vehicle power demand. A fuzzy inference system dynamically adjusts the weighting coefficients of these variables in real time, enabling continuous closed-loop EF regulation. The proposed strategy ensures optimal fuel cell operation while minimizing overall HC. The complete implementation architecture is illustrated in Figure 6.

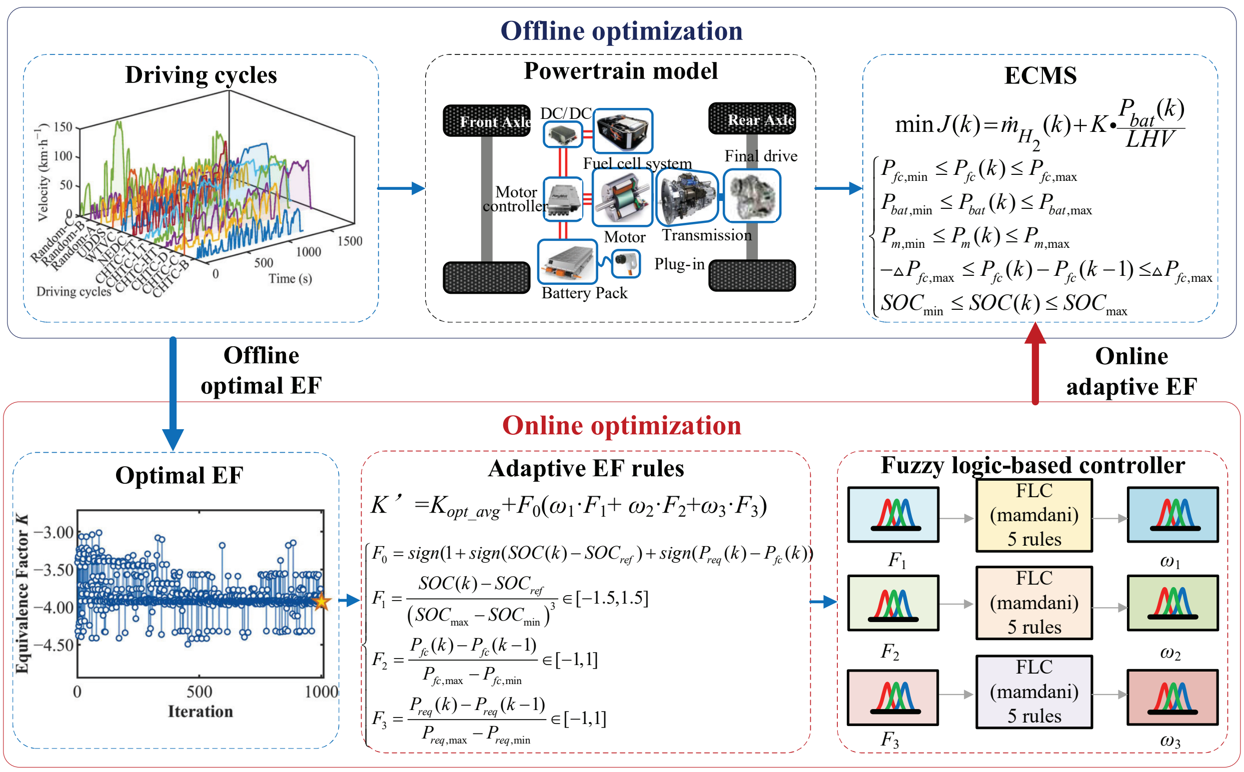


**Figure 6.** Architecture of the MFCA-ECMS.

In addition, the online adjustment of the EF depends on key vehicle parameters from Section 2. Battery SOC tracking ($F_1$) uses the rated capacity ($Q_{bat}$) and ampere-hour integration (Equation (6)). The normalization of features $F_2$ and $F_3$ is based on the limits of the FCS ($P_{fc,\max}$ and $P_{fc,\min}$) and the powertrain ($P_{req,\max}$ and $P_{req,\min}$). The FCS efficiency ($\eta_{fc}(P_{fc})$), shown in Figure 2, influences HC in the cost function (Equation (11)). Vehicle mass and dynamics impact the power demand ($P_{req}(k)$). Hence, the MFCA-ECMS process follows this sequence: parameters → feature extraction → fuzzy weighting → EF update → optimal power allocation.

### 3.1. ECMS Model of FCHECV

The ECMS is a widely used instantaneous optimization framework for energy management in fuel cell vehicles. Its core principle involves introducing an EF to convert the battery pack's instantaneous charge/discharge power into an equivalent HC. This transforms the overall energy optimization problem into a pointwise, sample-instantaneous minimization problem. Given the FCHECV's powertrain characteristics, this study optimizes instantaneous powertrain energy efficiency. Subject to power balance constraints, the instantaneous total equivalent HC—denoted as the objective function $J(k)$—is given by Equation (11):

$$\min J(k) = \dot{m}_{H_2}(k) + K \cdot \frac{P_{bat}(k)}{LHV} \tag{11}$$

In this equation, the parameter $K$ (the EF of ECMS) governs the real-time power distribution between the FCS and the battery, prioritizing electrical energy over hydrogen conversion. $P_{bat}(k)$ is positive during battery discharge and negative during charge. Under charging conditions (e.g., regenerative braking), the equivalent HC becomes negative, indicating energy recovery. The variable $k$ denotes the current sampling time, and the previous time step is implied where needed. All other physical quantities retain their previously defined meanings. In this study, the objective function minimizes only HC, omitting explicit battery aging terms. While the MFCA-ECMS indirectly protects the battery via SOC feedback ($F_1$) and power smoothing ($F_2$), future work will incorporate explicit aging constraints (e.g., charge/discharge rate, FCS power fluctuation) for multi-objective optimization [29,42]. In addition, all optimal EFs will be negative, following a sign convention opposite to the conventional ECMS: with $K < 0$, battery discharge ($P_{bat}(k) > 0$) reduces the total equivalent HC—rewarding the usage of battery energy—while charging increases it. Physically, discharging offsets real-time FCS energy demand, while charging incurs losses and cycle-life costs. Theoretically, the EF corresponds to the co-state in PMP, which can take negative values, especially at high battery SOC with strong discharging demand [44,45]. During optimization, the ECMS must adhere to multi-dimensional operational constraints to ensure that all powertrain components operate within their safety limits, as given by Equation (12):

$$\begin{cases} P_{fc,\min} \leq P_{fc}(k) \leq P_{fc,\max} \\ P_{bat,\min} \leq P_{bat}(k) \leq P_{bat,\max} \\ P_{m,\min} \leq P_m(k) \leq P_{m,\max} \\ SOC_{\min} \leq SOC(k) \leq SOC_{\max} \\ -\Delta P_{fc,max} \leq P_{fc}(k) - P_{fc}(k-1) \leq \Delta P_{fc,max} \end{cases} \tag{12}$$

In this equation, $P_{fc}(k)$, $P_{bat}(k)$, and $P_m(k)$ represent the instantaneous power outputs of the FCS, the battery power supply, and the drive motor, respectively. The operational ranges for each of these components are defined as $[P_{fc,\min}, P_{fc,\max}]$, $[P_{bat,\min}, P_{bat,\max}]$, and $[P_{m,\min}, P_{m,\max}]$, respectively. The term $SOC(k)$ denotes the battery's instantaneous SOC, with $SOC_{\min}$ and $SOC_{\max}$ denoting its minimum and maximum limits, respectively. Additionally, a ramp-rate constraint is imposed on the fuel cell output power between consecutive sampling instants to suppress severe fluctuations and ensure consistent evaluation of fluctuation suppression between the offline-optimized baseline EF and the proposed strategy.

### 3.2. Adaptive EF Regulation Framework

Owing to the diminished effectiveness of the conventional ECMS under stochastic driving conditions—and its failure to explicitly account for FCS operational stability constraints—this study proposes the MFCA-ECMS. Grounded in the structure of the traditional ECMS, the MFCA-ECMS establishes a rigorously formulated EF adaptation law, as given by Equation (13):

$$K' = K_{opt\_avg} + F_0(\omega_1 \cdot F_1 + \omega_2 \cdot F_2 + \omega_3 \cdot F_3) \tag{13}$$

In this equation, $K_{opt\_avg}$ denotes a baseline EF. The variable $F_0$ serves as the directional control factor, which governs the energy flow within the powertrain. Meanwhile, $F_1$, $F_2$, and $F_3$ denote the features used to quantify deviations in battery SOC, variations in FCS power, and fluctuations in vehicle power demand, respectively. The terms $\omega_1$, $\omega_2$, and $\omega_3$ correspond to the adaptive adjustment weights associated with $F_1$, $F_2$, and $F_3$, respectively.

In Equation (14), the directional factor $F_0$ is determined by both the battery's SOC and output power, taking values of $-1$, 0, or 1. Specifically, when the SOC exceeds the reference level ($SOC_{ref}$), $F_0$ becomes positive (allowing discharge). When the SOC falls below $SOC_{ref}$ and the output power is negative (e.g., during regenerative braking or external charging), $F_0$ becomes negative (inhibiting further discharge). The expression for $F_0$ is as follows:

$$F_0(k) = \begin{cases} +1 & SOC(k) \geq SOC_{ref} \\ -1 & SOC(k) < SOC_{ref} \text{ and } P_{bat}(k) < 0 \\ 0 & otherwise \end{cases} \tag{14}$$

In Equation (15), the feature quantity $F_1$ reflects the instantaneous deviation of battery SOC from its reference setpoint $SOC_{ref}$. To prevent accelerated degradation from deep discharges, $SOC_{ref}$ is conservatively set to 40%, in line with lithium-ion battery longevity guidelines. A cubic mapping is applied to nonlinearly scale the SOC error, enhancing closed-loop responsiveness near critical limits:

$$F_1(k) = \frac{\mathrm{SOC}(k) - \mathrm{SOC}_{ref}}{(\mathrm{SOC}_{\max} - \mathrm{SOC}_{\min})^3} \in [-1.5, 1.5] \tag{15}$$

In this paper, the battery SOC limits are set to $\mathrm{SOC}_{\max} = 90\%$ and $\mathrm{SOC}_{\min} = 20\%$. Accordingly, $\mathrm{SOC}_{ref} = 40\%$ and terminal SOC $\approx 20\%$. This design is justified based on safety, cycle life, and energy balance. The 20% limit prevents over-discharge (e.g., lithium plating), while the 90% upper bound avoids over-charge. Operating near 40% enables shallow cycling to reduce capacity fade, and the terminal 20% occurs only once per trip to minimize wear. Energy-wise, 20% reserves power for auxiliaries while maximizing hydrogen use, and 40% ensures stable tuning and SOC stability. These settings suppress degradation and ensure robust regulation [46].

In contrast, $F_2$ is a dynamic feature quantity derived from the rate of change in the FCS's power and serves as a metric for power fluctuations within the FCS. Large variations in FCS output power can accelerate performance degradation and compromise stability. The normalized definition of $F_2$ is presented in Equation (16):

$$F_2(k) = \frac{P_{fc}(k) - P_{fc}(k-1)}{P_{fc,\max} - P_{fc,\min}} \in [-1, 1] \tag{16}$$

where $P_{fc,\max} = 123.18\,\mathrm{kW}$ and $P_{fc,\min} = 5\,\mathrm{kW}$ are the maximum and minimum FCS output power limits derived from the FCS model in Section 2.2, respectively.

In Equation (17), the feature quantity $F_3$ represents a feedforward feature based on vehicle power demand variation. It characterizes both the trend and intensity of power demand fluctuations under unpredictable operating conditions. Due to inherent response delays, traditional feedback control struggles with rapid power distribution. To address this, the rate of power variation is introduced as feedforward information and normalized:

$$F_3(k) = \frac{P_{req}(k) - P_{req}(k-1)}{P_{req,\max} - P_{req,\min}} \in [-1, 1] \tag{17}$$

where $P_{req}(k)$ denotes the instantaneous vehicle power demand at discrete time step $k$; $P_{req,\max}$ and $P_{req,\min}$ represent the upper and lower bounds of the admissible power demand envelope, respectively, determined by the longitudinal dynamics model (Equation (1)) and the motor power limits (Equation (9)) presented in Section 2.

The adaptive adjustment mechanism described above endows the EF with dynamic state awareness, integrating offline-optimized control rules with real-time, state-dependent corrections. Notably, the adjustment weights $\omega_i$ ($i = 1, 2, 3$) are not static parameters; instead, they are computed online by the proposed FLC using the instantaneous feature quantities $F_i$ ($i = 1, 2, 3$). The normalization denominators for $F_2$ and $F_3$ are not empirical constants; rather, they are derived directly from the vehicle's physical limits: $P_{fc,\max}$, $P_{fc,\min}$, $P_{req,\max}$, and $P_{req,\min}$. These bounds reflect the inherent constraints of the FCS and the vehicle power demand, as specified in the corresponding design documentation [47,48]. The use of vehicle-specific physical bounds in the A-ECMS is further supported by recent work on universal EF bounds [49].

### 3.3. FLC Design

To facilitate real-time online adjustments to the adaptive EF, this section proposes a fuzzy-logic-based weight regulation scheme. Within each control cycle, the system first computes the adjustment weight $\omega_i$ via the fuzzy inference system using the instantaneous feature $F_i$; subsequently, the computed weights are substituted into Equation (13) to reconstruct the adapted EF $K'$ in real time.

#### 3.3.1. Membership Function Design

During fuzzification, this study employs a Gaussian-type MF, as given by Equation (18):

$$\mu(x) = \exp\left(-\frac{(x-c)^2}{2\sigma^2}\right) \tag{18}$$

where $x$ represents the precise value of the input feature quantity or the output weight, $c$ is the central value of this fuzzy subset, and $\sigma$ denotes the standard deviation of the control function's width. Compared with the conventional trapezoidal MF, the Gaussian function features smooth, differentiable boundaries, ensuring numerical continuity of the EF across operating condition transitions, and thereby suppressing transient oscillations in control commands.

As shown in Figure 7, the proposed fuzzy weight adjustment architecture utilizes a parallel configuration. The three feature quantities, $F_1$, $F_2$, and $F_3$, are independently input into dedicated fuzzy adjustment modules. Each module consists of a fuzzification unit, a rule inference engine, and a defuzzification unit. The input domain for each feature quantity is divided into five linguistic fuzzy subsets: NL (negative large), NS (negative small), ZO (zero), PS (positive small), and PL (positive large). The width parameters of the Gaussian MFs are adjusted individually to align with each feature quantity's dynamic behavior.

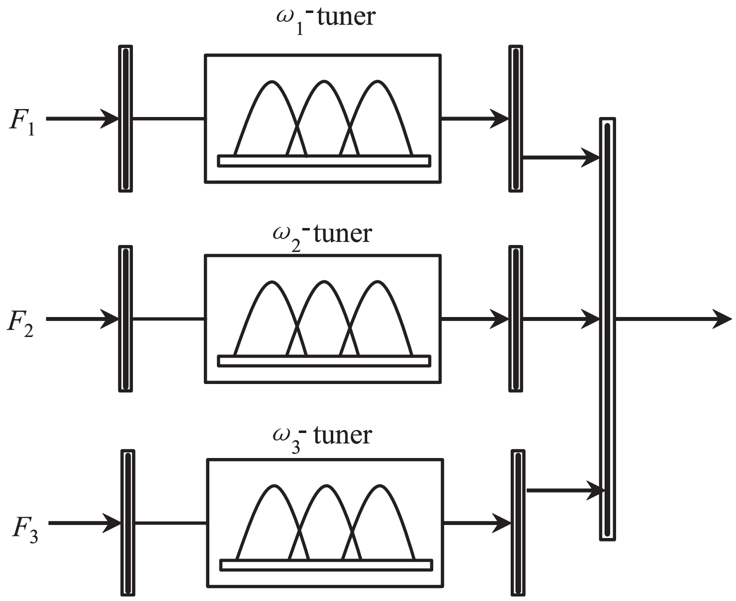


**Figure 7.** Architecture of fuzzy weight adjustment.

The primary goal of $F_1$ is to maximize electricity and hydrogen utilization, as well as to prevent over-discharge. To achieve this, a broad-support MF is employed. This design improves SOC stability during real driving cycles and helps avoid frequent charge-and-discharge that can result from excessive control sensitivity. As a result, the adjustment weight, denoted as $\omega_1$, is restricted to $[0, 1]$, reflecting its critical role in adaptive EF reconstruction.

For $F_2$, the MF parameters are intentionally set with a narrow support to improve responsiveness to FCS power fluctuations under uncertain operating conditions. This enables rapid detection and management of sudden power variations, thereby maintaining operational stability. Thus, the associated adjustment weight is limited to $\omega_2 \in [0, 0.5]$.

As a feedforward control term, $F_3$ is parameterized to capture the trends and intensities of power demand fluctuations arising from driver behavior. A narrow-width MF enables rapid detection of demand transients and facilitates real-time EF adjustment, thereby improving transient response and ensuring accurate power tracking. Accordingly, the adjustment weight is constrained to $\omega_3 \in [0, 0.3]$.

Based on the analysis, the fuzzy inference system's parameters have been finalized. The centers and widths of the MFs are systematically adjusted to produce the distribution shown in Figure 8. The left panel illustrates the input membership distributions, enabling a smooth transition from numerical values to linguistic fuzzy sets. The right panel shows the output membership distributions for the adjustment weights, where the universe of discourse is divided according to each weight's influence during adaptive adjustment. The specific values of the centers and widths of the Gaussian MFs are provided in Appendix B.

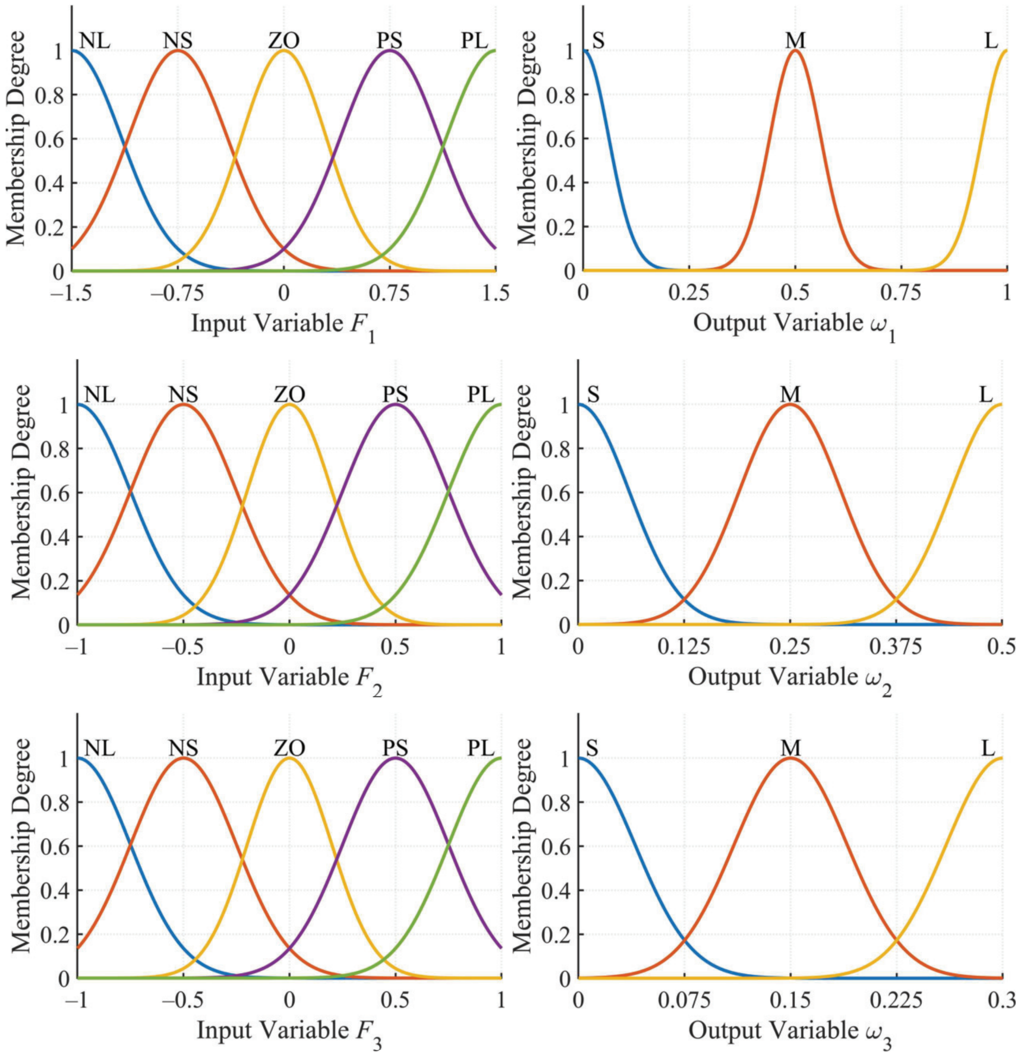


**Figure 8.** Membership functions for input and output variables.

### 3.3.2. Fuzzy Rules and Defuzzification

This section outlines a systematic set of fuzzy inference rules based on the previously established MFs. The main design principle is that control weights should change proportionally with both system deviation and volatility. Specifically, the weights increase as the system deviates further from the nominal operating range or experiences greater dynamic fluctuations, thereby enhancing regulatory responsiveness. Conversely, the weights decrease as the system approaches and maintains its desired operating state, promoting stability and reducing unnecessary interventions. The qualitative relationship between each weight and its corresponding system state variable is summarized in Table 1.

**Table 1.** Variation trend of fuzzy weights with system state.

| Operating Condition | $\omega_1$ | $\omega_2$ | $\omega_3$ |
|---|---|---|---|
| Large SOC deviation from $SOC_{ref}$ | Increase | No change | No change |
| Small SOC deviation from $SOC_{ref}$ | Decrease | No change | No change |
| Large FCS power variation | No change | Increase | No change |
| Small FCS power variation | No change | Decrease | No change |
| Severe vehicle power demand fluctuation | No change | No change | Increase |
| Mild vehicle power demand fluctuation | No change | No change | Decrease |

Based on these qualitative relationships, this paper develops a set of IF-THEN rules that link each feature quantity $F_i$ to its corresponding adjustment weight $\omega_i$. The detailed rules are presented in Table 2. It is worth noting that the fuzzy sets $\{L, M, S\}$ for the output weight $\omega_i$ correspond to the categories $\{large, medium, small\}$, respectively.

**Table 2.** Fuzzy rule base for weight adjustment

| No. | Input ($F_i$) | Output ($\omega_i$) | Explanation |
|---|---|---|---|
| 1 | NL | L | Strong negative deviation → large weight |
| 2 | NS | M | Slight negative deviation → medium weight |
| 3 | ZO | S | Near equilibrium → small weight |
| 4 | PS | M | Slight positive deviation → medium weight |
| 5 | PL | L | Strong positive deviation → large weight |

These fuzzy inference rules operationalize the dual design objectives of symmetric regulation and steady-state preservation. Specifically, for any deviation (positive or negative) in $F_i$, the corresponding adjustment weight $\omega_i$ exhibits a symmetric and monotonically increasing response with respect to the equilibrium point, ensuring rapid restoration of system equilibrium under substantial disturbances. Conversely, when the system is near equilibrium, $\omega_i$ is assigned a low value to mitigate unnecessary control actions and suppress power fluctuations induced by excessive EF fine-tuning.

Built on this unified design principle, the regulatory logic is applied consistently across the three input features: SOC deviation ($F_1$), FCS power variation ($F_2$), and vehicle power demand fluctuation ($F_3$). Each feature receives a larger weight when it significantly deviates from its target, while the other weights are reduced to minimize interference. All features compute weights using the same fuzzy rule base and collaborate to adjust the real-time EF. This coordinated mechanism optimizes battery depletion, controls fuel cell fluctuations, and tracks dynamic demand, fully aligning with the multi-feature coordination principle of the MFCA-ECMS.

After fuzzy reasoning, the system produces a fuzzy set as output. This paper uses the centroid method for defuzzification, which ensures continuity and smoothness of weight adjustment, as given by Equation (19):

$$\omega_i = \frac{\sum_{j=1}^{N} \mu_j c_j}{\sum_{j=1}^{N} \mu_j} \tag{19}$$

where $\omega_i$ represents the precise output value of the $i$-th adjustment weight. $N$ refers to the total number of fuzzy rules that are currently triggered. The symbol $\mu_j$ denotes the activation intensity of the $j$-th rule, and $c_j$ is the central value of the output fuzzy set that corresponds to this rule.

### 3.4. Algorithm Flow of MFCA-ECMS

In summary, the operational workflow of the MFCA-ECMS for determining real-time power distribution between the battery and FCS is illustrated in Figure 9. The procedure consists of the following sequential steps:

**Step 1: State Reading**

Read the vehicle power demand $P_{req}(k)$, battery SOC $\mathrm{SOC}(k)$, and FCS output power $P_{fc}(k)$ at the current time step $k$.

**Step 2: Adaptive EF Tuning**

Load the baseline optimal equivalence factor $K_{opt\_avg}$ and the reference SOC value $SOC_{ref}$. Calculate the directional factor $F_0(k)$ and the three characteristic quantities $F_1(k)$,

$F_2(k)$, and $F_3(k)$. Through fuzzy inference, obtain the adaptive adjustment weights $\omega_1(k)$, $\omega_2(k)$, and $\omega_3(k)$, and subsequently update the equivalence factor $K'(k)$.

**Step 3: Candidate Power Generation and Screening**

Discretely generate candidate FCS power within the allowable range and compute the corresponding battery power. Verify whether each candidate pair satisfies the predefined system constraints (e.g., power limits and SOC bounds).

**Step 4: Optimal Power Allocation and Execution**

For each feasible candidate, calculate the instantaneous equivalent HC objective. Select the candidate that minimizes the objective function as the optimal FCS output power, denoted as $P_{fc}^*(k)$. Compute the corresponding optimal battery power, denoted as $P_{bat}^*(k)$, based on the power balance equation.

**Step 5: Closed-Loop Iteration and Time Horizon Update**

Update the battery SOC to $SOC(k+1)$ using the optimal battery power. Advance the time step to $k = k + 1$ and return to Step 1 for the next sampling instant, thereby achieving closed-loop online optimization over the entire driving cycle.

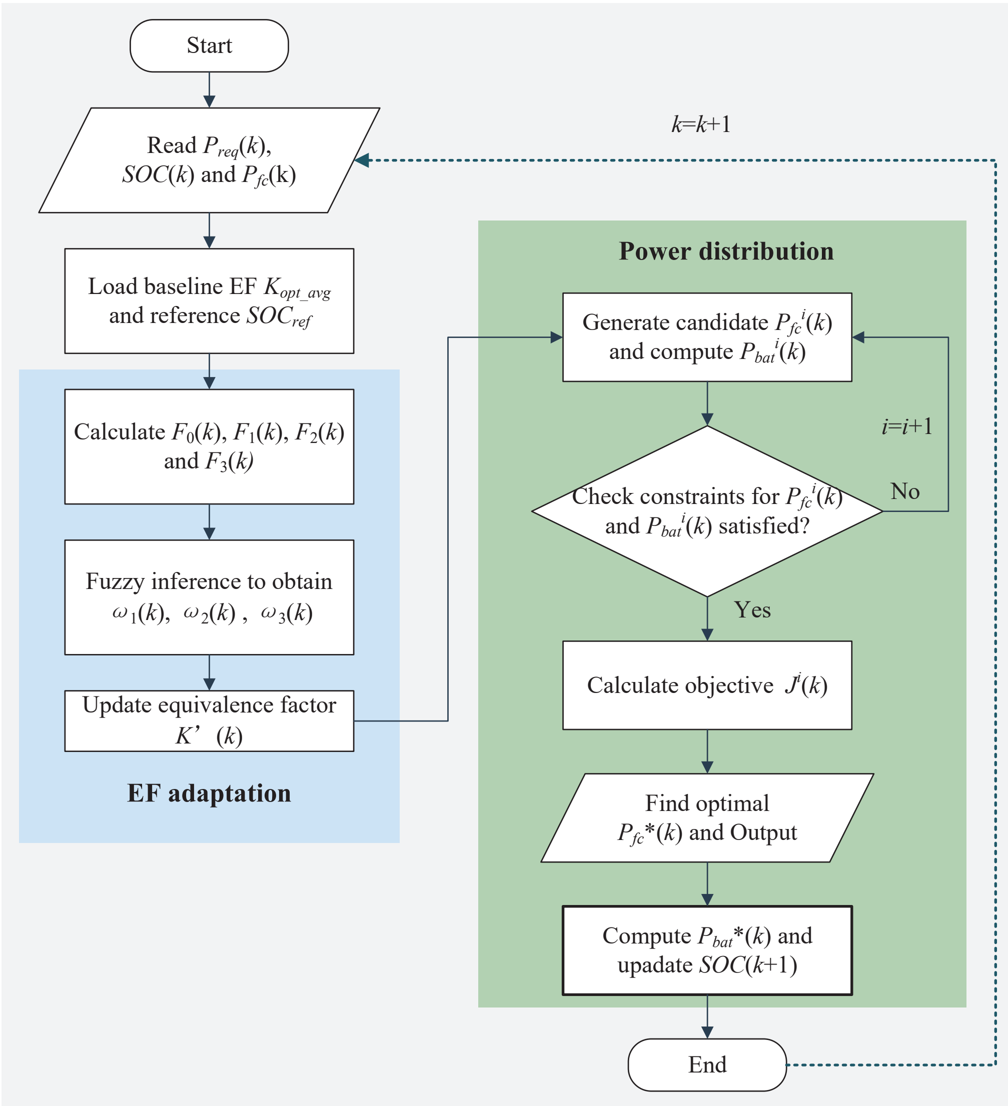


**Figure 9.** Flowchart of the MFCA-ECMS.

## 4. Results and Discussion

To thoroughly evaluate the performance of the proposed MFCA-ECMS, this section uses nine representative driving cycles and three stochastically generated cycles as test conditions. The representative cycles include the China heavy-duty commercial vehicle test cycles for bus (CHTC-B), coach (CHTC-C), dump truck (CHTC-D), tractor-trailer (CHTC-TT), trucks with a gross vehicle weight (GVW) greater than 5500 kg (CHTC-HT), and trucks with a GVW of 5500 kg or less (CHTC-LT). Additionally, the new European driving cycle (NEDC), the world transient vehicle cycle (WTVC), and the UDDS are included. The three stochastic cycles are labeled as Random-A, Random-B, and Random-C. The corresponding velocity–time profiles are illustrated in Figure 10.

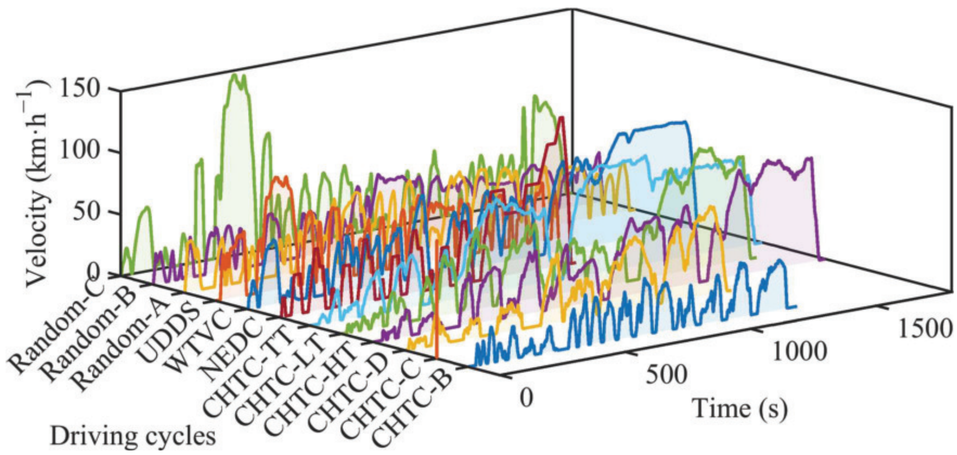


**Figure 10.** Test driving cycles.

Collectively, these cycles cover urban, suburban, and highway operational scenarios, capturing key dynamic characteristics, including frequent acceleration and deceleration, sustained cruising, load variations, and stochastic transitions in power demand. This comprehensive testbed enables realistic emulation of the transient and diverse operating environments encountered by FCHECVs in real-world scenarios.

### *4.1. Baseline EF*

The optimal EF in the ECMS determines the power split between the FCS and the battery, thereby significantly influencing vehicle economic performance. However, real-time calculation of the optimal EF is computationally challenging due to the inherently dynamic, time-varying nature of driving conditions. Previous studies have shown that, for vehicles with a fixed powertrain configuration, the optimal EF varies only slightly across operational scenarios [50]. Building on this insight, a baseline EF ($K_{opt\_avg}$) is first established within the proposed adaptive regulation framework. Specifically, $K_{opt\_avg}$ is calculated as the arithmetic mean of the theoretically optimal EFs derived from different driving cycles, as given by Equation (20):

$$K_{opt\_avg} = \frac{1}{n}\sum_{i=1}^{n} K_{opt,i} \tag{20}$$

where $K_{opt,i}$ represents the theoretical optimal EF for the $i$-th driving cycle.

This study employs the MIGA for offline optimization of the EF. By partitioning the population into isolated subpopulations—referred to as "islands"—and implementing a structured migration mechanism, the MIGA effectively enhances population diversity while mitigating premature convergence and reducing the risk of local optima. Consequently, it improves the robustness and reliability of global optimization for complex, nonlinear models. During optimization, the objective is to minimize the total equivalent HC, $J(k)$, while adhering to component power limits, SOC operating bounds, FCS ramp-rate limits, and a terminal SOC lower bound, without imposing an additional penalty for FCS power fluctuations. One critical requirement is the terminal battery SOC constraint, which stipulates that the SOC must not fall below approximately 20% at the end of each driving scenario. All compared strategies—DP, ECMS, CD-CS, and MFCA-ECMS—use the same initial SOC and a 20% terminal SOC lower bound to ensure fair comparison. This is essential for ensuring a balanced utilization of battery and FCS energy.

As illustrated in Figure 11, using the CHTC-C driving cycle as a representative example, the MIGA exhibits stable convergence throughout the optimization process. Figure 11a shows the convergence of the objective function. The value of $J(k)$ stabilizes after approximately 200 iterations, with the final change rate diminishing to less than 0.01%, satisfying the convergence criterion, and thereby confirming the algorithm's strong convergence capability. Figure 11b presents the evolutionary trajectory of the EF over 1000 iterations. Benefiting from the MIGA's global exploration mechanism, the initial search spans a broad region of the parameter space to ensure comprehensive coverage and avoid premature localization. Subsequently, the EF undergoes rapid refinement across an expanded search domain. As the optimization proceeds, the parameter distribution progressively narrows, culminating in precise convergence to the optimal value of $-3.95$, which is marked by the star in the figure.

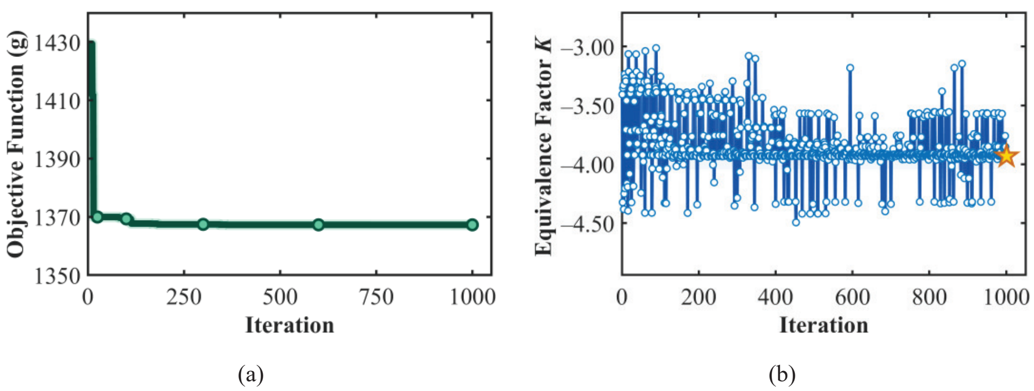


**Figure 11.** Optimization process @ CHTC-C: (**a**) convergence; (**b**) optimization trajectory.

To enhance the robustness and generalizability of the baseline EF, this study broadens the optimization beyond any single driving condition, as an EF derived from a single cycle may fail to account for variations across different operational scenarios. Accordingly, ten distinct driving cycles are employed to determine the baseline EF, including eight representative standard cycles and two stochastic cycles (Random-A and Random-B). These collectively cover urban, highway, and stochastic driving patterns, ensuring the robustness of $K_{opt\_avg}$ as a universally applicable baseline for real-time adaptive adjustment.

The process for acquiring the baseline EF is shown in Figure 12. The optimal EFs for each driving cycle, denoted $K_{opt,i}$, are determined, and their cumulative mean ($K_{opt\_avg,n}$) is examined. As shown, the $K_{opt\_avg,n}$ exhibits pronounced convergence as the number of driving cycles increases. Following an initial transient fluctuation, the mean curve rapidly asymptotes and stabilizes. The results indicate that, for $n \geq 3$, the rate of change in $K_{opt\_avg,n}$ remains below the predefined stability threshold of 2% and ultimately diminishes to just 0.01%. Furthermore, the coefficient of variation (CV) across the ten independent samples is 4.41%, which is well below the conventional 10% threshold widely used in statistical practice to indicate high data consistency. Accordingly, the arithmetic mean of the converged optimal EFs, $-3.8925$, is adopted as the baseline for real-time adaptive control.

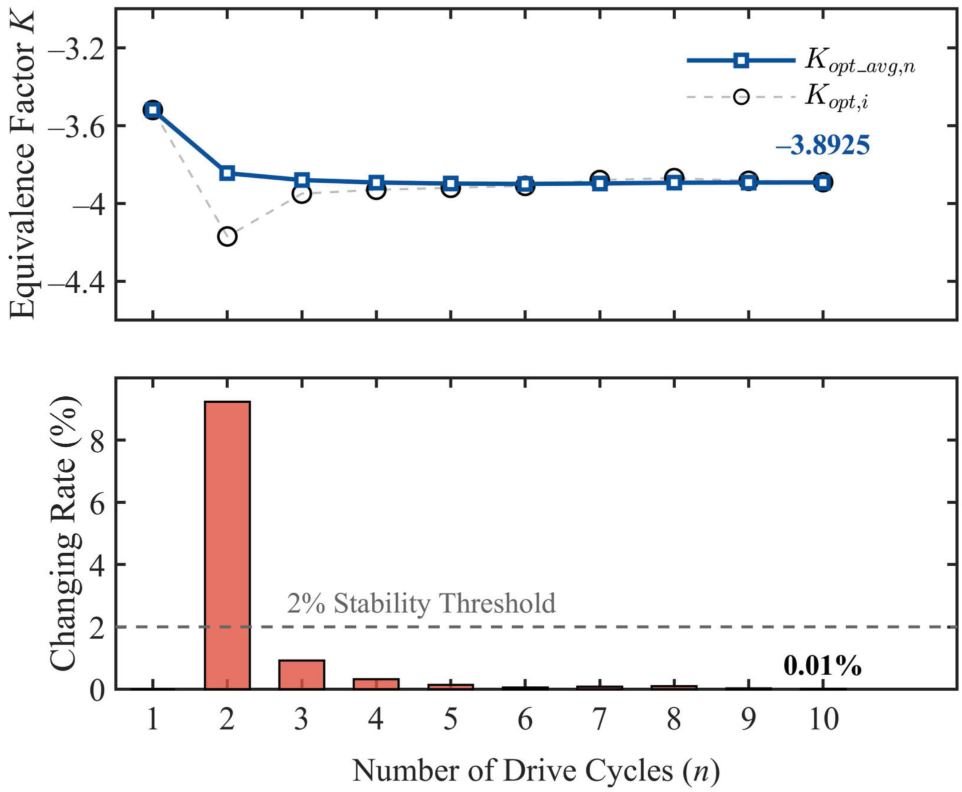


**Figure 12.** Baseline EF acquisition.

Table 3 presents the optimal EF values obtained under various operational scenarios. It also details fluctuations in the cumulative average EF observed during the baseline EF evaluation. Furthermore, the table includes relevant statistical details that provide insight into the reliability and significance of the findings. This comprehensive overview provides a clearer understanding of how different driving cycles affect EFs.

**Table 3.** Statistical analysis of the baseline EF.

| Items | Cycles | $K_{\mathbf{opt},i}$ | $K_{\mathbf{opt\_avg},n}$ | Changing Rate (%) | CVs (%) |
|---|---|---|---|---|---|
| 1 | CHTC-HT | −3.520 | −3.5200 | — | — |
| 2 | CHTC-TT | −4.170 | −3.8450 | 9.23 | 11.96 |
| 3 | CHTC-C | −3.950 | −3.8800 | 0.91 | 8.53 |
| 4 | WTVC | −3.930 | −3.8925 | 0.32 | 7.02 |
| 5 | CHTC-LT | −3.920 | −3.8980 | 0.14 | 6.22 |
| 6 | NEDC | −3.910 | −3.9000 | 0.05 | 5.67 |
| 7 | CHTC-D | −3.880 | −3.8971 | 0.07 | 5.25 |
| 8 | CHTC-B | −3.870 | −3.8938 | 0.09 | 4.93 |
| 9 | Random-A | −3.884 | −3.8927 | 0.03 | 4.66 |
| 10 | Random-B | −3.891 | −3.8925 | 0.01 | 4.41 |

### 4.2. Online Adaptation of the MFCA-ECMS

Figure 13 presents the online adaptation of key regulatory parameters in the MFCA-ECMS during the CHTC-C driving cycle. The four subfigures illustrate the operation of the proposed multi-feature collaborative regulation in four dimensions: (a) adaptive EF, (b) evolution of the direction factor and characteristic quantities, (c) dynamic allocation of adjustment weights, and (d) adjustment weights' responses to features.

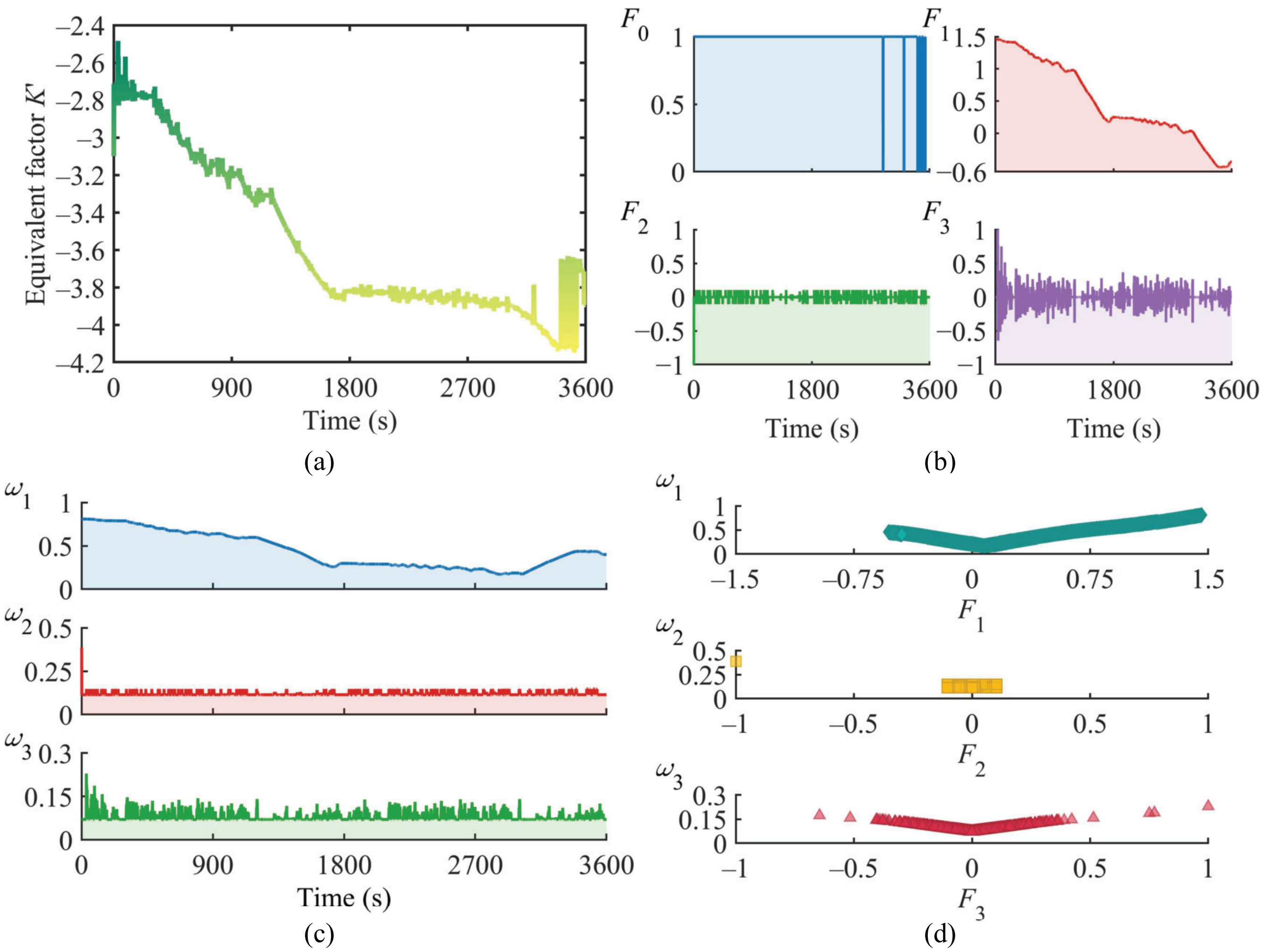


**Figure 13.** Regulatory parameters @ CHTC-C: (**a**) adaptive EF; (**b**) evolution of the features; (**c**) adjustment weights; (**d**) features vs. weights.

Figure 13a displays the temporal evolution of the adaptive EF. Initially, a pronounced downward trend suggests that greater regulatory intensity is needed to promote battery discharge at high SOC levels. This phase is followed by a quasi-stationary period, during which the EF stabilizes near a reference baseline. Toward the end, moderate fluctuations occur, corresponding to energy recovery of the power battery. This pattern demonstrates that the EF adapts in real time through nonlinear, state-dependent adjustments, underscoring the adaptability of the proposed strategy to regulatory changes.

Figure 13b illustrates the co-evolution of the direction factor and three feature quantities ($F_0$ to $F_3$) over time. In the initial phase, $F_0$ remains constant at 1. It then intermittently alternates between 0 and 1, reflecting a shift from continuous battery discharge to battery power maintenance. Concurrently, $F_1$ decreases steadily as the battery SOC declines, reflecting the gradual discharge of energy from the battery. $F_2$ initially exhibits significant fluctuations, followed by a brief transitional adjustment, after which it stabilizes with small-amplitude oscillations centered near . This pattern indicates that the MFCA-ECMS effectively reduces power fluctuations from the FCS. Meanwhile, $F_3$ exhibits persistent high-frequency oscillations, reflecting the strategy's capability to accurately capture rapid variations in vehicle power demand. Collectively, these features enable reliable detection of SOC deviations and transient power events, thereby establishing a robust basis for adaptive weight allocation.

Figure 13c illustrates the independent temporal trends of the three adjustment weights. Specifically, the evolution of $\omega_1$ can be delineated into three distinct phases, each closely aligned with the temporal profile of the EF $K'$. During Phase I, $\omega_1$ declines rapidly, reflecting an increasing emphasis on constraining battery discharge as the SOC depletes under multiple operational constraints. Next, in Phase II, which corresponds to the battery's charge-sustaining regime, $\omega_1$ remains comparatively stable and near-constant. Then, in Phase III, $\omega_1$ rises progressively, signifying a deliberate shift toward battery recharging and facilitating the recovery of stored energy. In contrast, since $F_2$ consistently exhibits only minor fluctuations, the temporal evolution of $\omega_2$ closely mirrors that of $F_2$. Meanwhile, $\omega_3$ exhibits significant initial fluctuations before stabilizing at a lower level. This trend reflects the rapid regulatory effect of the feedforward control term during transient responses.

Figure 13d illustrates the relationship between the weights and their corresponding features, highlighting a clear mapping. Feature 1 ($F_1$) shows a pronounced correlation with $\omega_1$. This weight changes monotonically with variations in $F_1$, thereby demonstrating the direct regulatory effect of SOC deviation on the predominant weight. For Feature 2 ($F_2$), in most cases, $F_2$ varies around ZO with a relatively small amplitude; thus, $\omega_2$ remains comparatively constant. However, at certain points where the variation in $F_2$ becomes significant (for example, when $F_2 = -1$), $\omega_2$ also increases, thereby rapidly adjusting the variation in $F_2$ back within the stable range. This behavior indicates a protective mechanism that limits extreme fluctuations in the FCS's power output. For Feature 3 ($F_3$), most values fall within the range $[-0.5, 0.5]$, with only a few operating points exhibiting significant sudden changes in vehicle power demand. From the trend of $\omega_3$, its relationship with $F_3$ is fundamentally similar to that between $\omega_1$ and $F_1$, both showing an obviously linear relationship.

The results confirm that the mapping between each weight $\omega_i$ and its corresponding feature $F_i$ adheres to the FLC design principles established in this work. In the positive half-region, $\omega_i$ increases as the feature quantity $F_i$ increases, thereby suppressing further increases in $F_i$. Conversely, in the negative half-region, $\omega_i$ increases as $F_i$ decreases, suppressing further decreases in $F_i$. This mechanism ensures that all three feature quantities remain within reasonable ranges, thereby guaranteeing slow discharge of the power battery while simultaneously suppressing sudden changes in FCS power.

### 4.3. Performance of the MFCA-ECMS

Three benchmark strategies were selected for comparison: DP provides the global optimal benchmark. Charge-depleting and charge-sustaining (CD-CS) represents a typical rule-based engineering method. The conventional ECMS with a fixed EF serves as the baseline for instantaneous optimization. The comparison covers HC, SOC trajectory, and FCS power fluctuation.

Figure 14 compares battery SOC trajectories and HC across four energy management strategies: DP, conventional ECMS, CD-CS, and the proposed MFCA-ECMS. The SOC trajectories of DP, MFCA-ECMS, and ECMS closely align, declining from 90% to 24%. In contrast, CD-CS ends slightly higher, at 24.72%, reflecting its rigid depletion–sustain logic, which prioritizes initial battery discharge and relies on FCS charging later, resulting in inefficient battery utilization. DP serves as the optimal benchmark, generating a smooth, nearly linear SOC decline through backward recursion based on a "uniform consumption" principle that minimizes hydrogen use. The MFCA-ECMS effectively tracks this reference trajectory through multi-feature collaborative regulation, which adjusts the EF based on SOC deviation, directional energy control, and feedforward compensation for demand fluctuations. The traditional ECMS, by contrast, relies on a fixed EF and performs adequately under steady conditions but struggles with high-frequency transients, leading to unexpected SOC deviations. Although the performance gap between the ECMS and MFCA-ECMS is modest under the moderately fluctuating CHTC-C cycle, the MFCA-ECMS demonstrates clear advantages in adaptability and responsiveness.

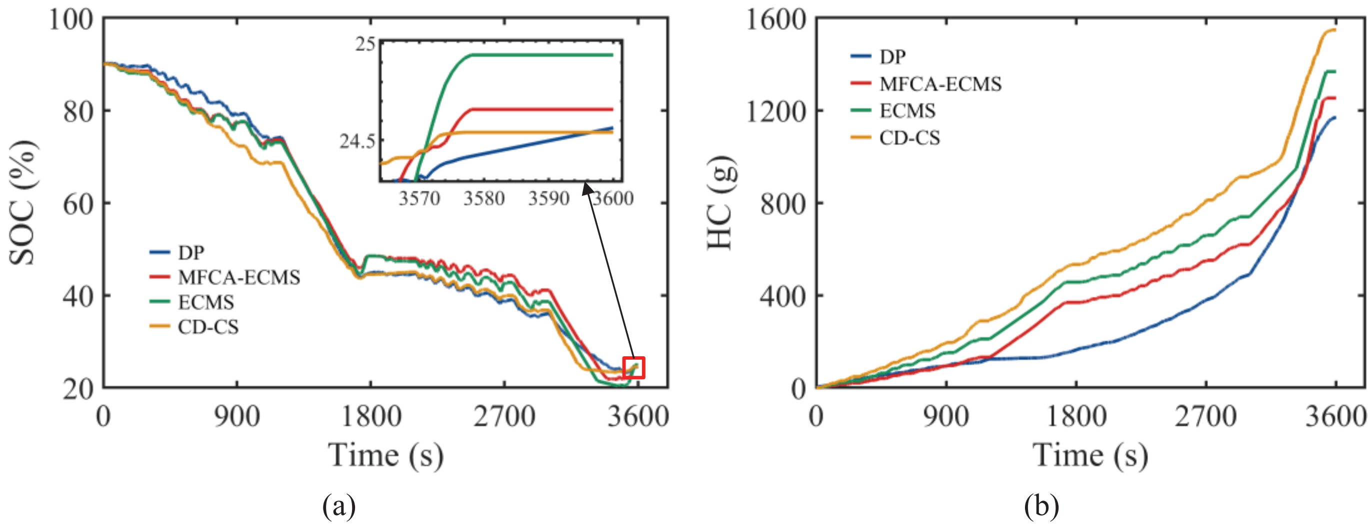


**Figure 14.** Battery SOC and HC @ CHTC-C: (**a**) battery SOC; (**b**) HC.

Regarding HC, DP achieves the lowest level (1170.07 g), followed closely by the MFCA-ECMS (1252.94 g), while the ECMS (1367.27 g) and CD-CS (1548.03 g) rank higher. However, DP is unsuitable for real-time applications because it relies on full prior knowledge of driving cycles. In contrast, the MFCA-ECMS adapts to unknown conditions using fuzzy inference to dynamically adjust the EF, incorporating SOC deviation, FCS power dynamics, and transient power demand. The adjustment weights $\omega_i$ help its SOC trajectory approach DP to promote energy efficiency, whilst suppressing FCS power fluctuations. On the other hand, the ECMS, with its fixed EF, cannot adapt in real time, leading to increased HC under dynamic conditions. Similarly, CD-CS suffers from a rigid power-management logic, particularly during the charge-sustaining phase, leading to the highest HC.

To verify the impact of the MFCA-ECMS on FCS durability, Figure 15 illustrates the distribution of power change rates for the four strategies. It should be noted that the present study uses the statistical distribution of FCS power variation rates as an indirect proxy for transient-induced degradation. For more accurate durability assessment, future work could incorporate advanced methods, such as polarization-loss decomposition-based online health-state estimation [51], which enables quantitative decoupling of activation, ohmic, and concentration losses.

The results indicate that while the power change rate distributions under the four strategies all show a similar trend, their specific patterns differ significantly. For instance, CD-CS appears scattered, with lower representation in the low-variation range and higher in the high-variation range, indicating pronounced power fluctuations. In contrast, DP serves as a global optimal benchmark with a more uniform distribution; however, because it emphasizes energy consumption optimization, it results in lower low-variation rates. Similarly, the ECMS shows a pattern close to that of DP but with a slightly higher proportion in the low-variation range, suggesting better control over power fluctuations. Finally, the MFCA-ECMS closely resembles DP but exhibits a notably higher proportion in the low-variation range and minimized high-variation rates, demonstrating its effectiveness in reducing power fluctuations.

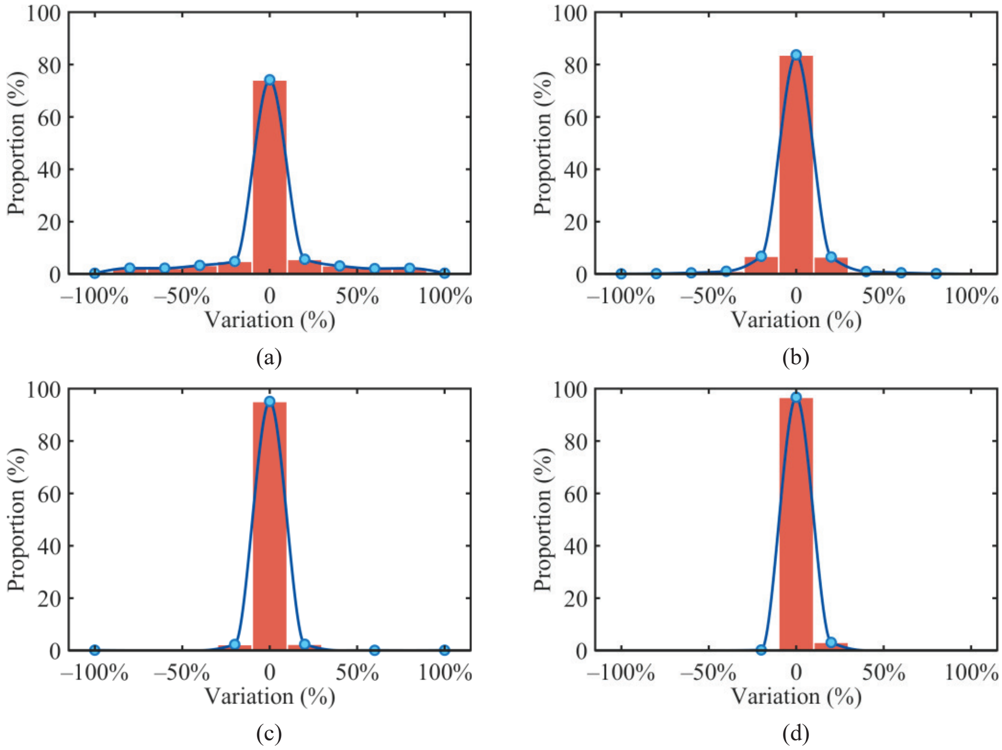


**Figure 15.** Distribution of the FCS's power variation @ CHTC-C: (**a**) CD-CS; (**b**) DP; (**c**) ECMS; (**d**) MFCA-ECMS.

Table 4 presents a comparative analysis of four EMSs evaluated under the CHTC-C driving cycle, with an initial SOC of 90%. DP exhibits the lowest HC, at 1170.07 g, and the greatest HC savings improvement, at 24.56%, compared to CD-CS. However, its FCS power variation rate remains within ±10% at only 83.74%, which could compromise the FCS's longevity over time. In contrast, the MFCA-ECMS consumes 1252.94 g of hydrogen, achieving a 19.06% improvement while demonstrating the highest power variation rate within ±10%, at 99.75%. This indicates superior management of power fluctuations. The ECMS displays moderate performance, consuming 1367.27 g with an 11.68% improvement and a power fluctuation suppression rate of 95.19%. Conversely, CD-CS performs least effectively, consuming 1548.03 g and achieving only 74.22% suppression, due to its rigid operational logic. In summary, the MFCA-ECMS successfully balances fuel economy and FCS durability, achieving near-optimal hydrogen efficiency while maintaining superior fuel cell longevity compared to DP.

**Table 4.** Comparisons of four strategies @ CHTC-C.

| Strategy | Initial SOC (%) | Terminal SOC (%) | HC (g) | Improvement (%) | Proportion of the Change Rate in FCS Power Within ±10% (%) |
|---|---|---|---|---|---|
| CD-CS | 90 | 24.54 | 1548.03 | — | 74.22 |
| ECMS | 90 | 24.94 | 1367.27 | 11.68 | 95.19 |
| MFCA-ECMS | 90 | 24.66 | 1252.94 | 19.06 | 99.75 |
| DP | 90 | 24.56 | 1170.07 | 24.56 | 83.74 |

### 4.4. Further Verification

To verify the generalization ability and robustness of the MFCA-ECMS across different driving conditions, independent tests were conducted using the Random-C driving cycle (independent of baseline acquisition conditions and better reflecting real-world randomness) and the UDDS cycle (results provided in Appendix C). Two initial SOC levels were evaluated: 90% (fully charged) and 45% (typical mid-level charge).

4.4.1. Initial Battery SOC @ 90% Under Random-C

Figure 16 presents the variation in adaptive parameters with an initial SOC of 90%. Specifically, as shown in Figure 16a, the EF decreased from approximately −2.6 to −3.8 during the first 2700 s due to the relatively high energy reserve of the power battery. As the battery's stored electrical energy diminishes, the system transitions into a power-maintenance phase. During this phase, to optimize power consumption and fuel efficiency, the MFCA-ECMS continuously adjusts the EF to maintain a dynamic equilibrium between charging and discharging the battery. As a result, sustained EF fluctuations are observed after 2700 s, demonstrating the MFCA-ECMS's responsiveness to operational disturbances. This process is further supported by the temporal evolution of $F_0$ and $F_1$ in Figure 16b. Before approximately 2700 s, $F_0$ remained constant at unity, while $F_1$ declined monotonically, resulting in a continuous reduction in EF and promoting battery discharge. After 2700 s, $F_0$ alternated cyclically between 1 and 0 to regulate and sustain the battery's SOC, while $F_1$ stabilized near −0.6, further validating the effectiveness of the proposed control strategy. Regarding $F_3$, the vehicle power demand exhibited periodic variation, with amplitude and frequency modulated by real-time operating conditions. Additionally, $F_2$ remained within a narrow operational band, indicating minimal control effort and directly contributing to enhanced durability and extended service life of the FCS. Figure 16c reveals distinct temporal evolution patterns among the adaptive weights: $\omega_1$ exhibits a gradual decline over the time interval of 0 to 2700 s, then increases gradually and converges to a steady state—characterized by low-amplitude oscillations—by approximately 4000 s; $\omega_2$ undergoes rapid initial adaptation and achieves convergence to a quasi-steady regime with minimal fluctuations, closely tracking the dynamics of $F_2$; $\omega_3$ exhibits high-fidelity tracking of $F_3$ across the entire time horizon. Figure 16d quantifies the functional relationships: each adjustment weight exhibits a piecewise linear dependence on its corresponding feature parameter. In the negative domain, the feature and weight vary inversely; in the positive domain, they vary proportionally. This mapping enhances transient responsiveness and control sensitivity.

Figure 17 illustrates the battery SOC and hydrocarbon HC under the four control strategies. All strategies commence with an initial SOC of 90% and converge to approximately 24%. Prior to ∼1800 s, the SOC trajectories exhibit close agreement across all strategies. Beyond this point, CD-CS yields the steepest SOC decline, followed by the ECMS; in contrast, the MFCA-ECMS closely tracks the DP benchmark, indicating superior optimality in powertrain energy distribution. With respect to HC, CD-CS exhibits the largest deviation from the DP reference, the ECMS the second largest, and the MFCA-ECMS the smallest, demonstrating its enhanced energy-saving potential.

Figure 18 presents the distribution of FCS power change rates. In alignment with the CHTC-C results, CD-CS exhibits the broadest distribution, which reflects low temporal concentration and high variability in power transitions. While DP achieves optimal HC reduction, its offline and non-causal implementation inherently results in substantial FCS power fluctuations. In contrast, the ECMS markedly reduces transient power excursions. Importantly, the MFCA-ECMS demonstrates the narrowest distribution, with most rate values remaining within physically feasible and operationally safe limits—a result attributable to its online adaptive EF tuning.

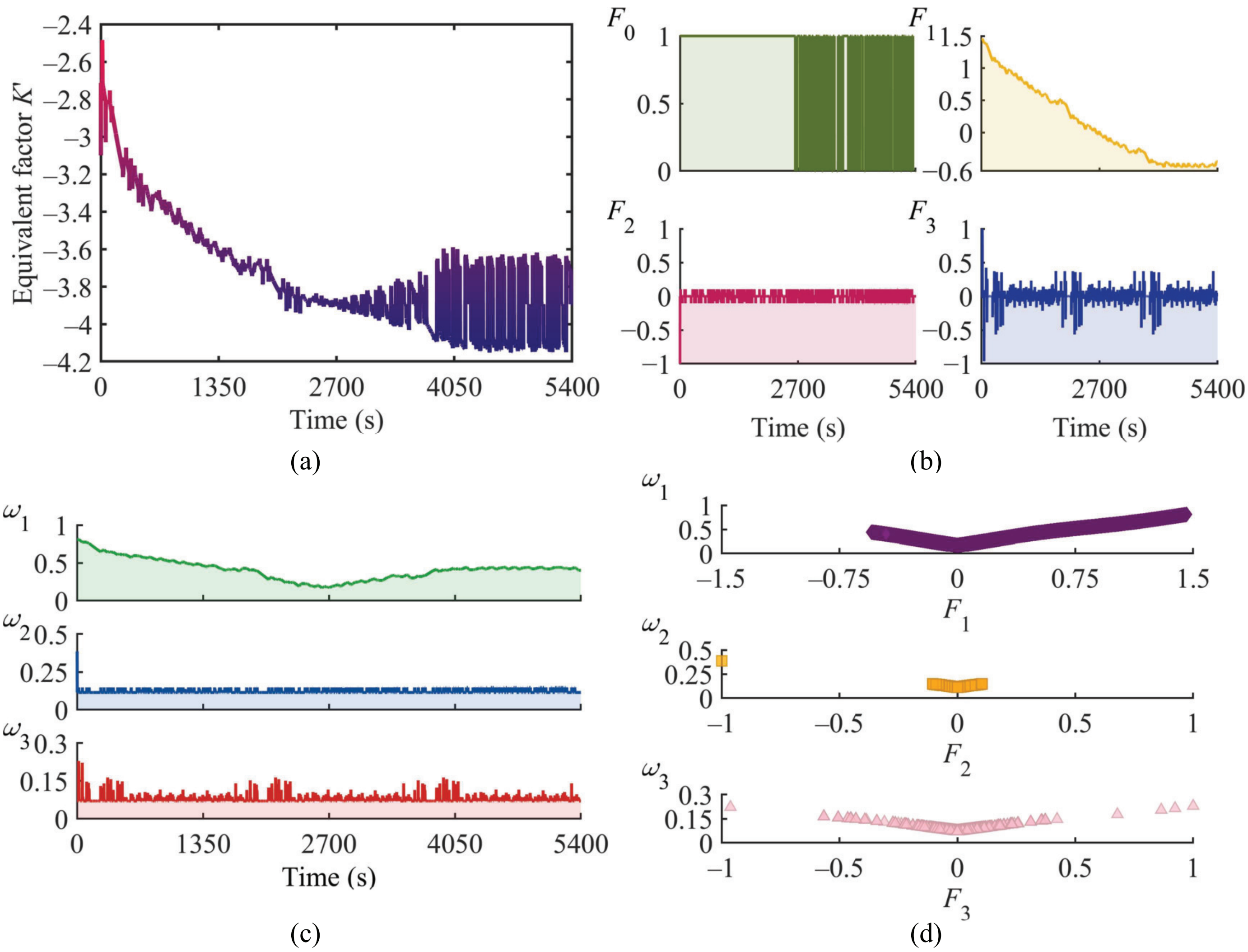


**Figure 16.** Regulatory parameters @ Random-C (initial SOC = 90%): (**a**) adaptive EF; (**b**) evolution of the features; (**c**) adjustment weights; (**d**) features vs. weights.

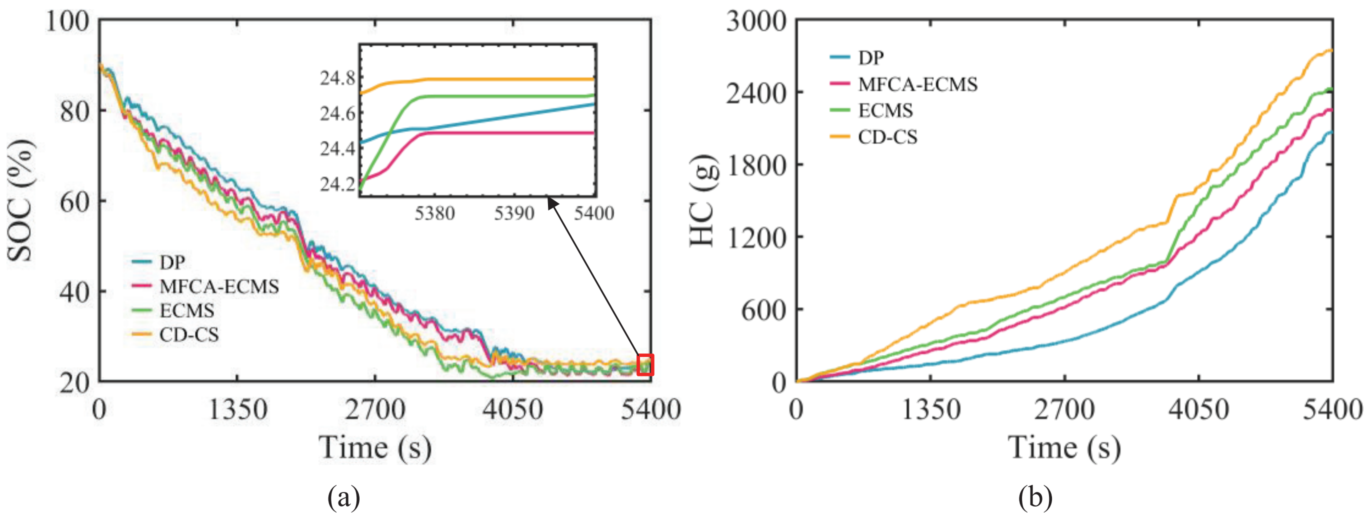


**Figure 17.** Battery SOC and HC @ Random-C (initial SOC = 90%): (**a**) battery SOC; (**b**) HC.

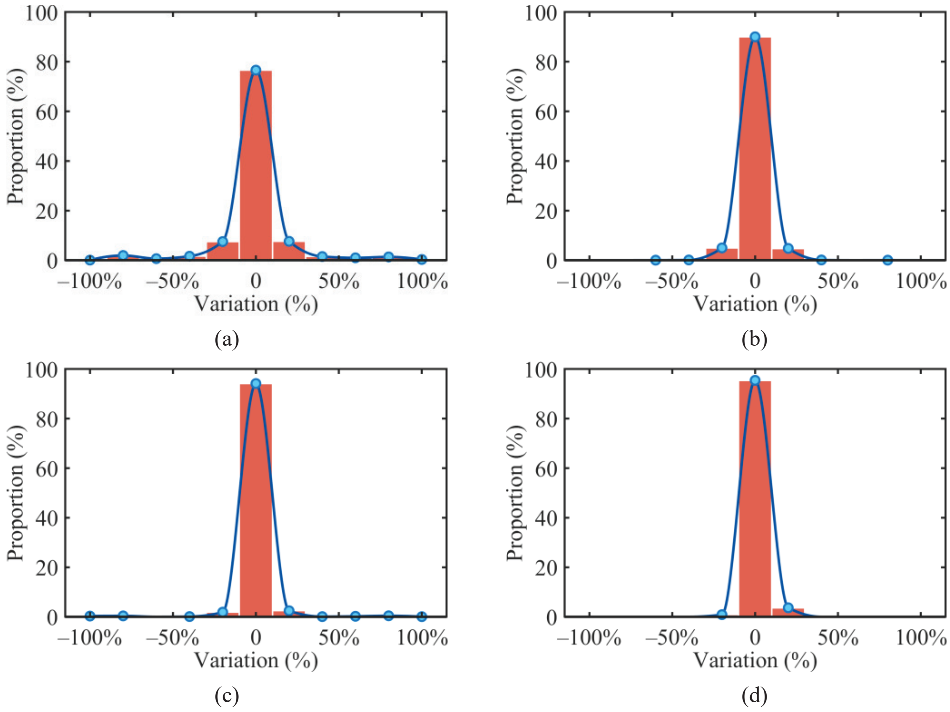


**Figure 18.** Distribution of the FCS's power variation @ Random-C (initial SOC = 90%): (**a**) CD-CS; (**b**) DP; (**c**) ECMS; (**d**) MFCA-ECMS.

4.4.2. Initial Battery SOC @ 45% Under Random-C

To assess effectiveness under a standardized mid-level charge, identical tests were performed with an initial SOC of 45%. The results are presented in Figures 19–21. As shown in Figure 19a, the EF did not decrease significantly with lower SOC; instead, EF exhibited a rapid initial adjustment, followed by minor fluctuations and then pronounced volatility as the battery transitioned to a power-maintenance phase. Figure 19b provides additional detail: Approximately 500 s into the test, $F_0$ alternates between 1 and 0, dynamically changing the direction of energy flow. At the same time, $F_1$ fluctuates in accordance with the battery's power-maintenance stage, gradually decreasing from its initial value and then oscillating with reduced amplitude after about 2000 s. Meanwhile, $F_2$ remains consistent with the 90% SOC scenario and, during this period, effectively mitigates the decline in FCS performance. $F_3$ shows changes that align with previous data, maintaining established transition patterns throughout the observation period. Turning to Figure 19c, $\omega_2$ and $\omega_3$ largely correspond to the 90% SOC scenario. However, $\omega_1$ displays notable differences: after a brief decrease, it increases and stabilizes near 0.5 after about 2000 s. Finally, Figure 19d demonstrates that the correlations between $F_2$ and $\omega_2$, and between $F_3$ and $\omega_3$, remain consistent with the 90% SOC scenario. The correlation between $F_1$ and $\omega_1$ continues to be linear across both ranges, although the operational point is primarily in the negative range. Collectively, these findings indicate that a low initial SOC has negligible influence on $F_2$ and $F_3$ but exerts a pronounced effect on $F_1$, thereby substantiating that adaptive adjustment of $\omega_1$ effectively maintains battery power balance and prevents excessive discharge. These systematic differences align with each feature's functional design: $\omega_2$ and $\omega_3$ respond only to real-time FCS fluctuations and demand transients, independent of the initial SOC, whereas $\omega_1$ strengthens regulation under low initial SOC to prevent excessive discharge. This differentiated logic demonstrates the strategy's strong adaptation to varying initial battery states and verifies the robustness of the coordinated adaptive mechanism across multiple features.

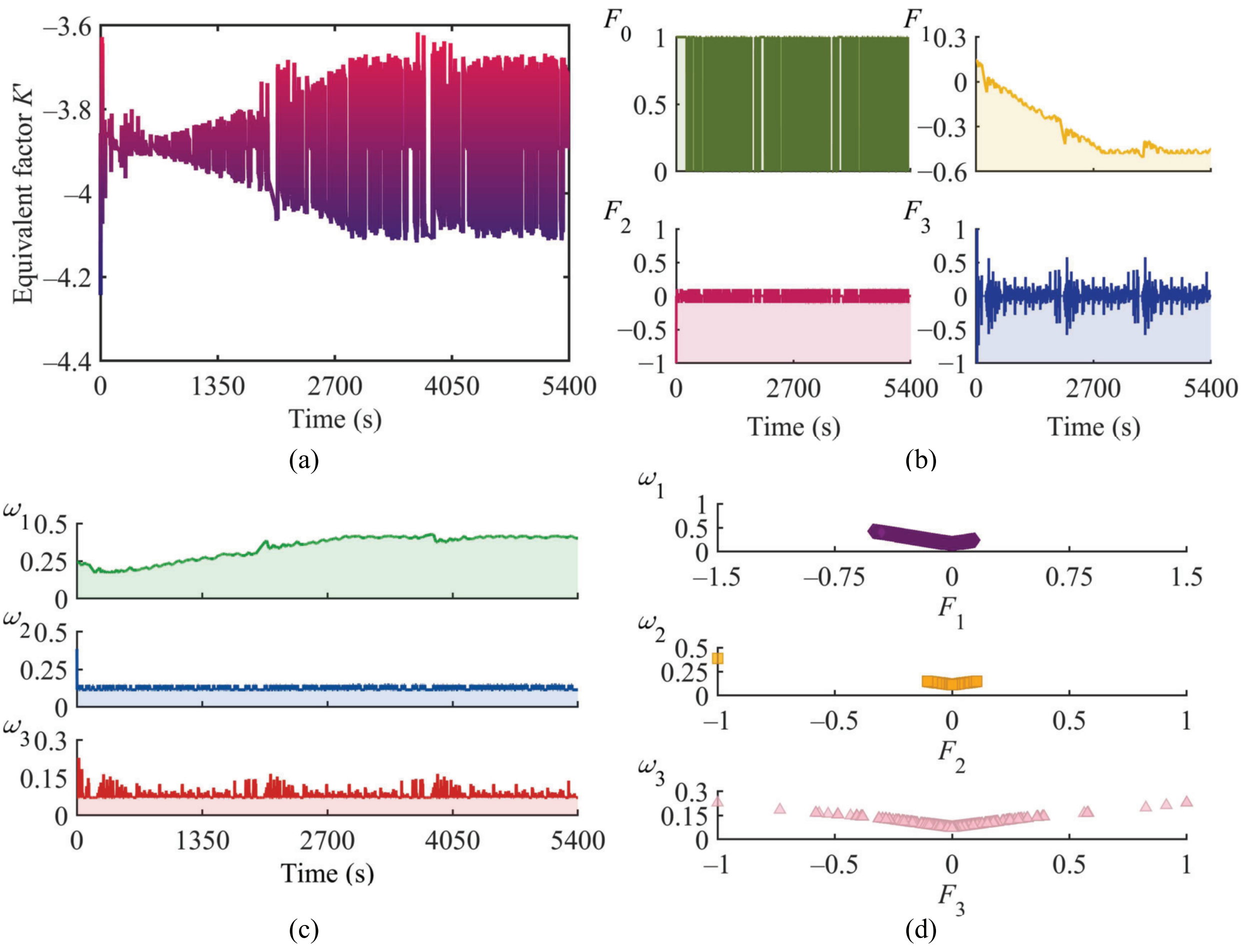


**Figure 19.** Regulatory parameters @ Random-C (initial SOC = 45%): (**a**) adaptive EF; (**b**) evolution of the features; (**c**) adjustment weights; (**d**) features vs. weights.

Figure 20 illustrates the changes in battery SOC and HC across four different strategies. It is evident that DP, based on global energy consumption optimization, results in the SOC trajectory decelerating the most slowly. By the end of the operation, it reaches the battery's discharge limit, ensuring optimal global energy consumption. In contrast, the other three real-time strategies show different rates of battery power consumption. CD-CS consumes the most battery power and enters the maintenance stage after approximately 1000 s, resulting in the highest HC. The traditional ECMS employs a fixed EF, resulting in lower power consumption than CD-CS; however, it consumes battery power more quickly than the DP strategy, indicating a lower average energy-saving potential. In comparison, the MFCA-ECMS can perform online adaptive adjustments to the EF through multi-feature coordination. The results are significant, where the SOC decelerates more slowly and closely resembles DP. Additionally, in terms of HC, the MFCA-ECMS outperforms both CD-CS and the traditional ECMS.

Figure 21 illustrates the distribution of the FCS's power-changing rate across the four control strategies at an initial battery SOC of 45%. The overall distribution patterns closely resemble those observed at the higher initial SOC of 90%, indicating consistent qualitative behavior across SOC levels. Among the strategies, CD-CS exhibits the lowest proportion of change rates falling within the target band (±10%), followed by DP. In contrast, both the conventional ECMS and MFCA-ECMS demonstrate improved regulation of change rates—particularly the MFCA-ECMS, which incorporates real-time FCS dynamics into its adaptive EF tuning mechanism. This enables a substantially more favorable distribution of change rates, with a markedly higher concentration within the ±10% band.

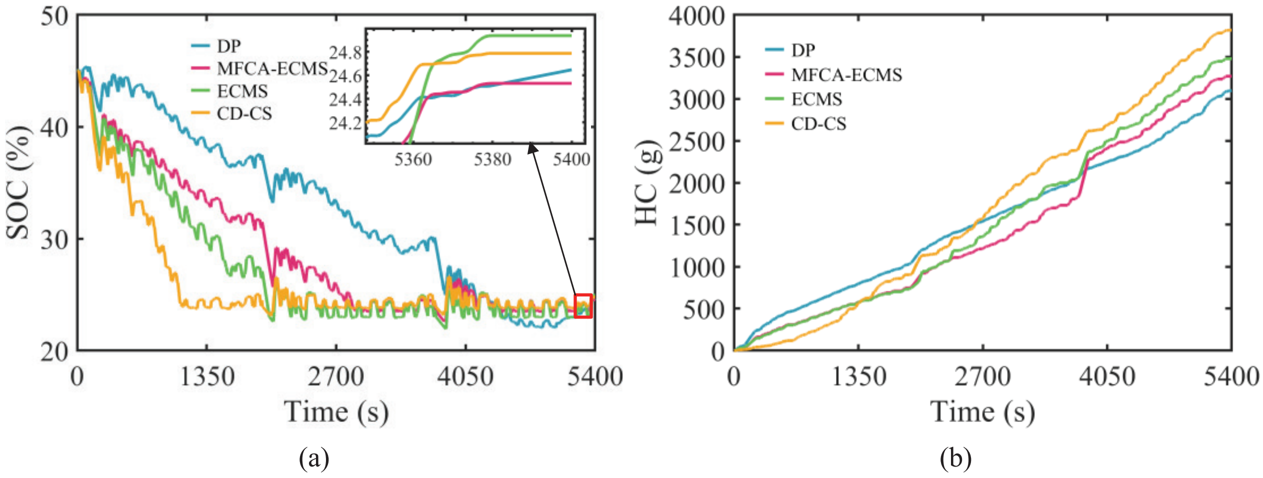


**Figure 20.** Battery SOC and HC @ Random-C (initial SOC = 45%): (**a**) battery SOC; (**b**) HC.

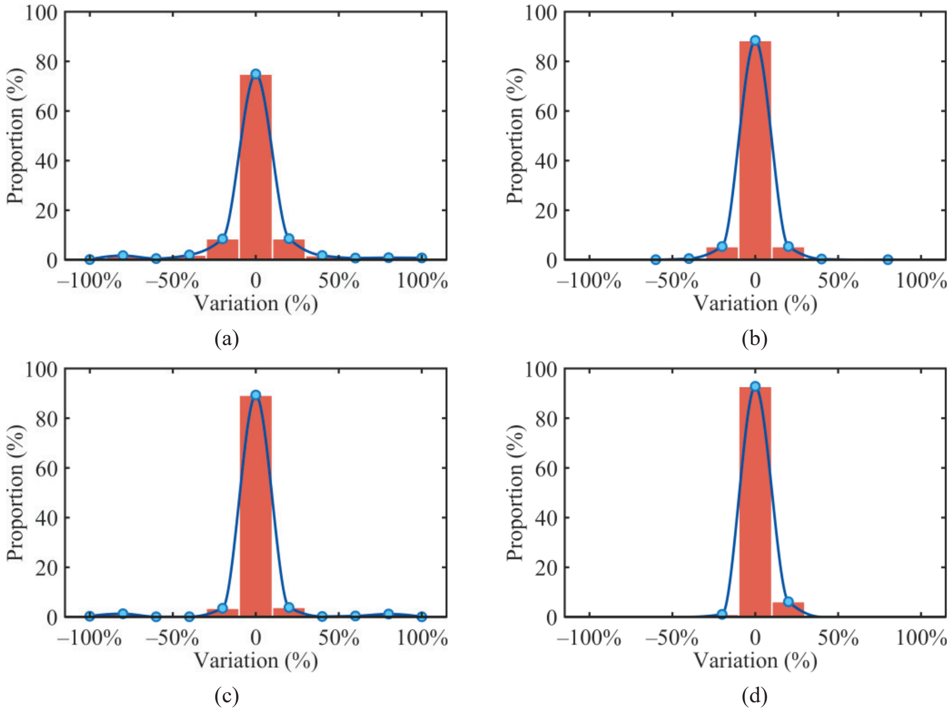


**Figure 21.** Distribution of the FCS's power variation @ Random-C (initial SOC = 45%): (**a**) CD-CS; (**b**) DP; (**c**) ECMS; (**d**) MFCA-ECMS.

Nevertheless, a notable degradation in the FCS's power-changing rate suppression performance is observed across all four strategies relative to the 90% SOC case. This attenuation stems primarily from the earlier onset of the battery's charge-sustaining phase due to the reduced initial SOC. As a result, the battery's ability to buffer transient power demands diminishes, leading to larger and more frequent FCS fluctuations in response to abrupt changes in vehicle power demand.

Table 5 summarizes the performance of different strategies under Random-C and UDDS cycles (UDDS results are detailed in Appendix C). The results indicate that, under varying operating conditions, the proposed MFCA-ECMS demonstrates superior performance across all evaluated metrics compared to both the ECMS and CD-CS, with outcomes marginally higher than those of DP in terms of HC. Specifically, analyzing two distinct initial battery SOCs within Random-C reveals that HC is 17.98% and 14.38% lower than under CD-CS, respectively. In the UDDS, HC is 18.73% and 13.45% lower than under CD-CS, respectively. Consequently, the data support the conclusion that the initial SOC influences the energy-saving effectiveness of the MFCA-ECMS; notably, a higher initial SOC yields a more pronounced energy-saving impact. The other three strategies exhibit a similar trend. In terms of minimizing the rate of change in FCS power, the MFCA-ECMS consistently outperforms the alternatives across both operating scenarios. When comparing different initial SOCs, the proportion of the FCS power change rate governed by the MFCA-ECMS within the ideal range is 98.65% and 98.20%, respectively, in Random-C; in the UDDS, these figures are 98.70% and 97.61%, respectively. Although the initial SOC does exert an influence, its effect remains relatively minor in this context.

**Table 5.** Performance of control strategies under different driving cycles.

| Cycles | Strategy | Initial SOC (%) | Terminal SOC (%) | HC (g) | Improvement (%) | Proportion of the Change Rate in FCS Power Within ±10% (%) |
|---|---|---|---|---|---|---|
| Random-C | CD-CS | 90 | 24.78 | 2744.60 | — | 76.61 |
| | ECMS | 90 | 24.76 | 2425.43 | 11.63 | 94.19 |
| | MFCA-ECMS | 90 | 24.38 | 2251.13 | 17.98 | 98.65 |
| | DP | 90 | 24.65 | 2071.89 | 24.51 | 90.06 |
| | CD-CS | 45 | 24.79 | 3817.69 | — | 74.96 |
| | ECMS | 45 | 24.76 | 3477.27 | 8.92 | 89.37 |
| | MFCA-ECMS | 45 | 24.53 | 3268.57 | 14.38 | 98.20 |
| | DP | 45 | 24.65 | 3099.21 | 18.82 | 88.50 |
| UDDS | CD-CS | 90 | 22.91 | 2974.90 | — | 82.79 |
| | ECMS | 90 | 22.84 | 2608.19 | 12.33 | 93.97 |
| | MFCA-ECMS | 90 | 22.42 | 2417.61 | 18.73 | 98.70 |
| | DP | 90 | 22.07 | 2235.22 | 24.86 | 89.05 |
| | CD-CS | 45 | 22.94 | 4084.53 | — | 80.72 |
| | ECMS | 45 | 22.50 | 3724.54 | 8.81 | 88.92 |
| | MFCA-ECMS | 45 | 22.68 | 3535.14 | 13.45 | 97.61 |
| | DP | 45 | 22.26 | 3265.88 | 20.04 | 83.52 |

The fact that over 97% of power fluctuations remain within the mild range has significant physicochemical implications for fuel cell durability. Sharp power swings cause abrupt current density changes, accelerating platinum catalyst dissolution, carbon support corrosion, and membrane humidity cycling that leads to mechanical fatigue and chemical degradation—processes well recognized as primary drivers of PEMFC lifetime decay [52]. By confining the vast majority of power transitions to a benign range, the MFCA-ECMS fundamentally mitigates these adverse degradation pathways, providing a solid basis for subsequent quantitative lifespan extension evaluation [53]. The MFCA-ECMS, while not as optimal as the DP global optimum, significantly reduces HC compared to CD-CS. DP's offline and non-causal nature requires full knowledge of the driving cycle, making it impractical for real-time control. In contrast, the MFCA-ECMS operates online using current measurements and adjusts the EF in real time, prioritizing feasibility over optimality. This approach effectively suppresses FCS power fluctuations, enhancing stack durability. Overall, it achieves a good balance among hydrogen economy, real-time feasibility, and fuel cell lifetime.

## 5. Conclusions

This paper proposes a fuzzy-logic-based MFCA-ECMS for FCHECVs. The strategy integrates battery SOC, FCS power dynamics, and vehicle power demand. The main findings are as follows:

(1) The MFCA-ECMS consistently reduces HC across different initial SOC levels and driving cycles. Under Random-C with 90% initial SOC, the HC reductions are 17.98% vs. CD-CS and 7.19% vs. the conventional ECMS; under the UDDS, they are 18.73% and

7.31%, respectively. At 45% initial SOC, the reductions are 14.38%/6.00% on Random-C and 13.45%/5.09% on the UDDS, confirming robust fuel-economy improvements.

(2) The three-feature synergy (SOC feedback $F_1$, FCS power variation $F_2$, and feedforward demand $F_3$) keeps over 97% of FCS power change rates within $\pm$10% (up to 98.70%), versus only 89–94% for the conventional ECMS, confirming its effectiveness in mitigating transient-induced degradation.

(3) Several limitations are acknowledged: simulations under standard conditions only (no extreme temperatures, complex terrain, or battery aging); expert-dependent fuzzy rules requiring real-world validation; and no detailed degradation model—only qualitative lifespan inference from power fluctuation suppression.

(4) Future work will explore deep RL for automated fuzzy rule generation, conduct HIL and real-vehicle tests, couple the strategy with validated fuel cell degradation and battery aging models for multi-objective optimization, and integrate V2X technology for predictive energy management.

**Author Contributions:** Conceptualization, X.Z. and X.L. (Xiaodong Liu); methodology, X.Z., X.L. (Xiaodong Liu), and J.D.; software, X.Z. and X.J.; validation, J.D. and X.L. (Xiaorui Li); formal analysis, X.Z.; investigation, X.Z. and X.L. (Xiaodong Liu); data curation, X.Z.; writing—original draft preparation, X.Z.; writing—review and editing, X.L. (Xiaodong Liu), J.D. and X.L. (Xiaorui Li); visualization, X.Z. and X.J. All authors have read and agreed to the published version of the manuscript.

**Funding:** This research was funded in part by the Innovation Capability Enhancement Initiative for Technology-Oriented SMEs of Shandong Province 2024PDJH38/K24LB9601, and in part by the Doctoral Scientific Research Foundation of Liaocheng University 318052058.

**Institutional Review Board Statement:** Not applicable.

**Informed Consent Statement:** Not applicable.

**Data Availability Statement:** The data presented in this study are available upon request from the corresponding author.

**Conflicts of Interest:** The authors declare no conflicts of interest.

## Abbreviations

The following abbreviations are used in this manuscript:

*Acronyms*

| | |
|---|---|
| A-ECMS | Adaptive Equivalent Consumption Minimization Strategy |
| AMT | Automated Manual Transmission |
| ANFIS | Adaptive Neuro-Fuzzy Inference System |
| BEV | Battery Electric Vehicle |
| BP | Backpropagation |
| CD-CS | Charge-Depleting and Charge-Sustaining |
| CHTC-B | China Heavy-Duty Commercial Vehicle Test Cycle for Bus |
| CHTC-C | China Heavy-Duty Commercial Vehicle Test Cycle for Coach |
| CHTC-D | China Heavy-Duty Commercial Vehicle Test Cycle for Dumper |
| CHTC-HT | China Heavy-Duty Commercial Vehicle Test Cycle for Heavy Truck |
| CHTC-LT | China Heavy-Duty Commercial Vehicle Test Cycle for Light Truck |
| CHTC-TT | China Heavy-Duty Commercial Vehicle Test cycle for Tractor-trailer |
| CV | Coefficient of Variation |
| DDPG | Deep Deterministic Policy Gradient |
| DDQN | Double Deep Q-Networks |
| DP | Dynamic Programming |
| DQL | Deep Q-Learning |
| EF | Equivalent Factor |

| | |
|---|---|
| ECMS | Equivalent Consumption Minimization Strategy |
| EMS | Energy Management Strategy |
| FCEV | Fuel Cell Electric Vehicle |
| FCHECV | Fuel Cell Hybrid Electric Commercial Vehicle |
| FCS | Fuel Cell System |
| FL | Fuzzy Logic |
| FLC | Fuzzy Logic Controller |
| GVW | Gross Vehicle Weight |
| HC | Hydrogen Consumption |
| MF | Membership Function |
| MFCA-ECMS | Multi-Feature Coordinated Adaptive Equivalent Consumption Minimization Strategy |
| MIGA | Multi-Island Genetic Algorithm |
| MPC | Model Predictive Control |
| NEDC | New European Driving Cycle |
| NL | Negative Large |
| NS | Negative Small |
| PEMFC | Proton-Exchange Membrane Fuel Cell |
| PI | Proportional–Integral |
| PL | Positive Large |
| PMP | Pontryagin's Minimum Principle |
| PMSM | Permanent-Magnet Synchronous Motor |
| PS | Positive Small |
| RL | Reinforcement Learning |
| SOC | Battery State of Charge |
| UDDS | Urban Dynamometer Driving Schedule |
| WTVC | World Transient Vehicle Cycle |
| ZO | Zero |
| *Symbols* | |
| $m$ | Vehicle's mass (kg) |
| $g$ | Gravitational acceleration (m·s$^{-2}$) |
| $f$ | Rolling friction coefficient |
| $C_d$ | Aerodynamic drag coefficient |
| $\rho_{air}$ | Air density (kg·m$^{-3}$) |
| $A_f$ | Frontal surface area (m$^2$) |
| $\delta$ | Rotational mass correction coefficient |
| $u$ | Vehicle velocity (m·s$^{-1}$) |
| $\alpha$ | Road slope (°) |
| $du/dt$ | Vehicle's acceleration (m·s$^{-2}$) |
| $P_{req}$ | Vehicle required power (kW) |
| $P_{bat}$ | Battery power (kW) |
| $P_{fc}$ | Output power of the FCS (kW) |
| $\Delta SOC$ | The SOC variation |
| $LHV$ | Lower heating value of hydrogen (J·g$^{-1}$) |
| $T_{AMT\_out}$ | Output torque of the AMT (N·m) |
| $T_{AMT\_in}$ | Input torque of the AMT (N·m) |
| $n_{AMT\_out}$ | AMT's output rotational speeds (rad/s) |
| $n_{AMT\_in}$ | AMT's input rotational speeds (rad/s) |
| $i_g$ | Speed ratio of the AMT |
| $\eta_{AMT}$ | Efficiency of the AMT across various speed ratios |
| $P_m$ | Motor output power (kW) |
| $T_m$ | Motor torque (N·m) |
| $\eta_m$ | Motor efficiency |

## Appendix A. Vehicle Parameters

**Table A1.** Powertrain parameters of the studied FCHECV.

| System | Parameter | Symbol | Value |
|---|---|---|---|
| Vehicle | Vehicle mass | $m$ | 25,000 kg |
| | Rolling friction coefficient | $f$ | 0.018 |
| | Aerodynamic drag coefficient | $C_d$ | 0.53 |
| | Ambient air density | $\rho_{air}$ | 1.23 kg·m$^{-3}$ |
| | Frontal surface area | $A_f$ | 8.37 m$^2$ |
| | Gravitational acceleration | $g$ | 9.81 m·s$^{-2}$ |
| | Road slope | $\alpha$ | 0° |
| FCS | Peak power | $P_{fc,\max}$ | 123.18 kW |
| | Rated power | $P_{fc}$ | 120 kW |
| | Minimum power | $P_{fc,\min}$ | 5 kW |
| Battery | Nominal capacity | $Q_{bat}$ | 100 A·h |
| | Rated voltage | $U_{bat}$ | 523 V |
| Motor | Peak power | $P_{m,\max}$ | 320 kW |
| | Peak speed | $n_{m,\max}$ | 3400 r·min$^{-1}$ |
| | Peak torque | $T_{m,\max}$ | 2200 N·m |
| AMT | Speed ratio | $i_g$ | 8.456/4.913/2.976/1.915/1.238/1.000/0.97 |
| | Efficiency | $\eta_{AMT}$ | 0.96 |

## Appendix B. Parameters of the Fuzzy Logic Controller for MFCA-ECMS

**Table A2.** The Specifics of the Gaussian Membership Function Parameters.

| Variable | Fuzzy Subsets | Centers $c$ | Widths $\sigma$ |
|---|---|---|---|
| $F_1$ | NL, NS, ZO, PS, PL | $[-1.5, -0.75, 0, 0.75, 1.5]$ | $[0.35, 0.35, 0.3, 0.35, 0.35]$ |
| $F_2$ | NL, NS, ZO, PS, PL | $[-1, -0.5, 0, 0.5, 1]$ | $[0.25, 0.25, 0.2, 0.25, 0.25]$ |
| $F_3$ | NL, NS, ZO, PS, PL | $[-1, -0.5, 0, 0.5, 1]$ | $[0.25, 0.25, 0.2, 0.25, 0.25]$ |
| $\omega_1$ | S, M, L | $[0, 0.5, 1]$ | $[0.06, 0.06, 0.06]$ |
| $\omega_2$ | S, M, L | $[0, 0.25, 0.5]$ | $[0.06, 0.06, 0.06]$ |
| $\omega_3$ | S, M, L | $[0, 0.15, 0.3]$ | $[0.04, 0.04, 0.04]$ |

## Appendix C. Results for UDDS

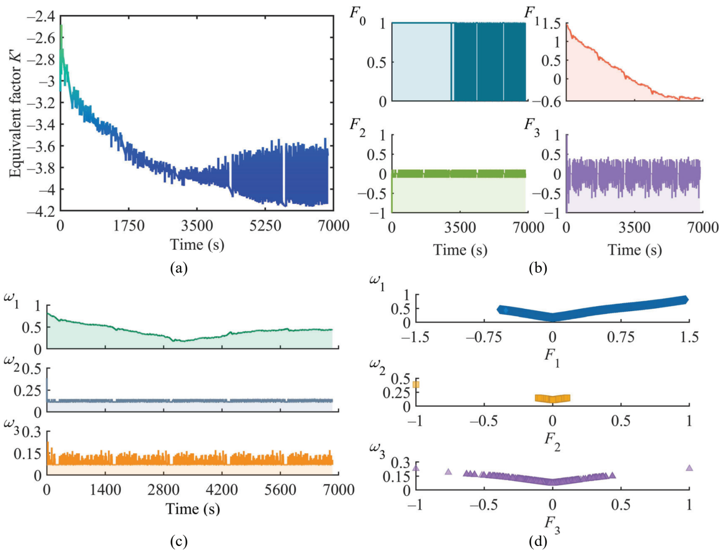


**Figure A1.** Regulatory parameters @ UDDS (initial SOC = 90%): (**a**) adaptive EF; (**b**) evolution of the features; (**c**) adjustment weights; (**d**) features vs. weights.

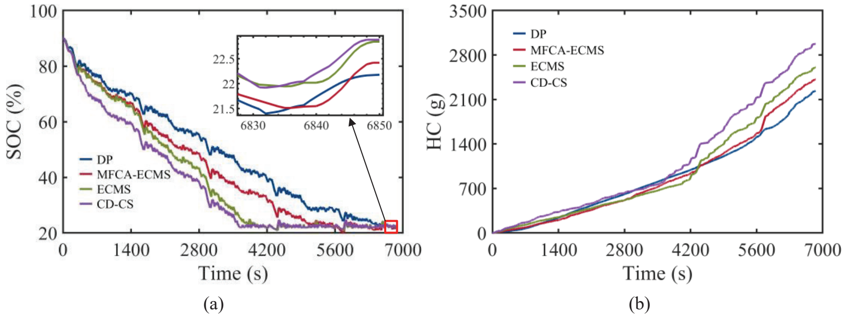


**Figure A2.** Battery SOC and HC @ UDDS (initial SOC = 90%): (**a**) battery SOC; (**b**) HC.

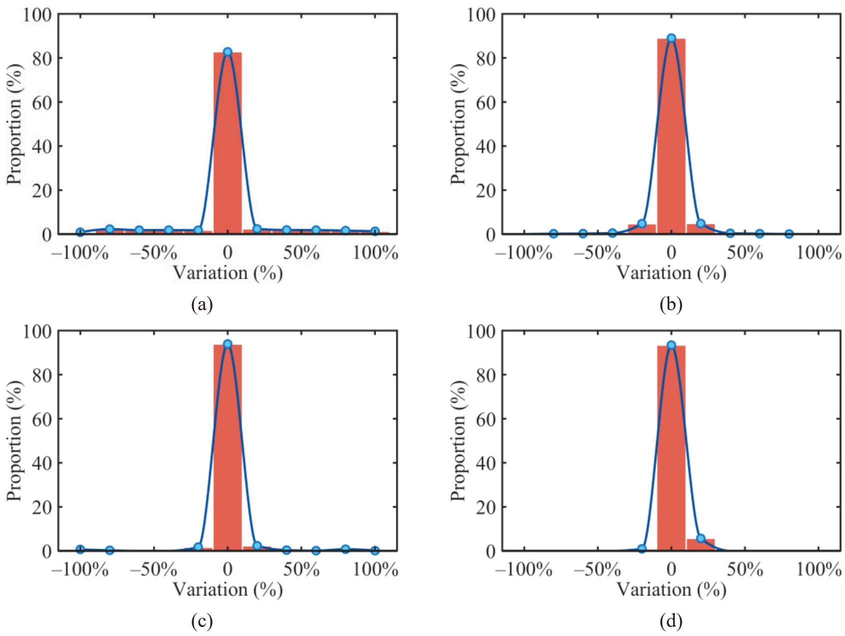


**Figure A3.** Distribution of the FCS's power variation @ UDDS (initial SOC = 90%): (**a**) CD-CS; (**b**) DP; (**c**) ECMS; (**d**) MFCA-ECMS.

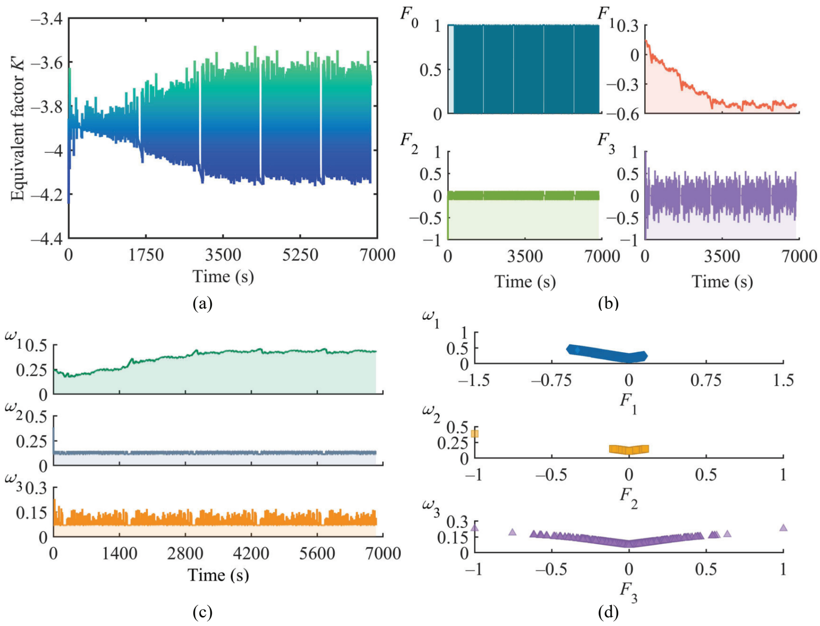


**Figure A4.** Regulatory parameters @ UDDS (initial SOC = 45%): (**a**) adaptive EF; (**b**) evolution of the features; (**c**) adjustment weights; (**d**) features vs. weights.

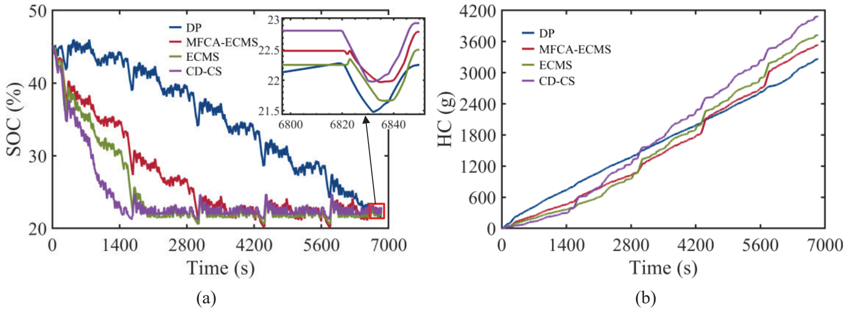


**Figure A5.** Battery SOC and HC @ UDDS (initial SOC = 45%): (**a**) battery SOC; (**b**) HC.

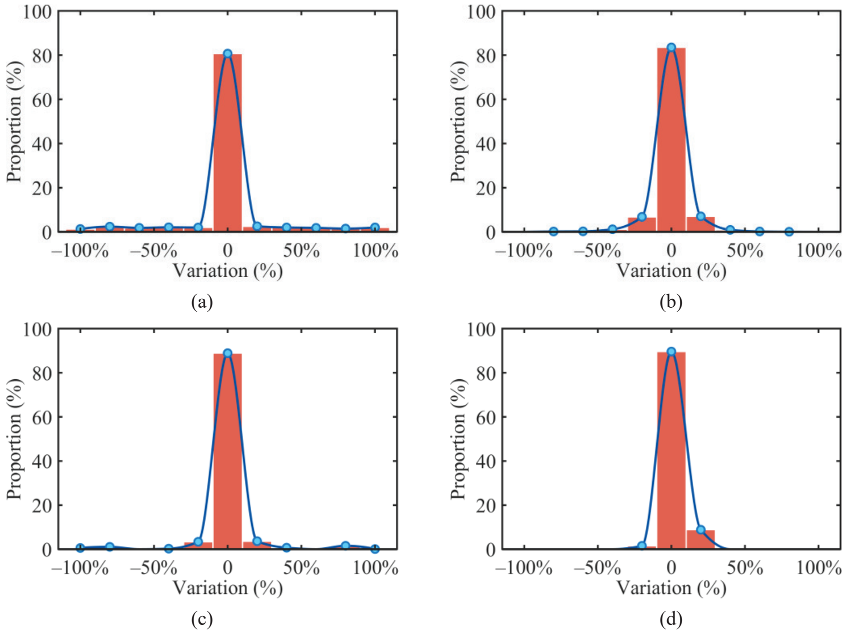


**Figure A6.** Distribution of the FCS's power variation @ UDDS (initial SOC = 45%): (**a**) CD-CS; (**b**) DP; (**c**) ECMS; (**d**) MFCA-ECMS.

## References


1. Sun, D.; Kyere, F.; Sampene, A.K.; Asante, D.; Kumah, N.Y.G. An Investigation on the Role of Electric Vehicles in Alleviating Environmental Pollution: Evidence from Five Leading Economies. *Environ. Sci. Pollut. Res.* **2022**, *30*, 18244–18259. [CrossRef]
2. Zhang, Z.; Song, G.; Li, Y.; Wang, W.; Wang, S.; He, S.; Wang, J. A Review: Research on Molecular Dynamic Behavior of Hydrate-Based Hydrogen Storage. *Int. J. Hydrogen Energy* **2026**, *202*, 152922.
3. Zeng, Q.H.; He, L.Y. Study on the Synergistic Effect of Air Pollution Prevention and Carbon Emission Reduction in the Context of "dual Carbon": Evidence from China's Transport Sector. *Energy Policy* **2023**, *173*, 113370. [CrossRef]
4. Bai, F.; Zhao, F.; Liu, M.; Liu, Z.; Hao, H.; Reiner, D.M. Assessing the Viability of Renewable Hydrogen, Ammonia, and Methanol in Decarbonizing Heavy-duty Trucks. *Appl. Energy* **2025**, *383*, 125293. [CrossRef]
5. Deng, Y.; Ma, M.; Zhou, N.; Ma, Z.; Yan, R.; Ma, X. China's Plug-in Hybrid Electric Vehicle Transition: an Operational Carbon Perspective. *Energy Convers. Manag.* **2024**, *320*, 119011. [CrossRef]
6. Lv, Z.; Guo, J.; Mao, H.; Dong, Y. Experimental Analysis of Energy Flow and Carbon Dioxide Emissions in Plug-in Hybrid Electric Vehicles under Different Operation Modes. *Energy Convers. Manag.* **2025**, *343*, 120223. [CrossRef]
7. Hu, H.; Yuan, W.W.; Su, M.; Ou, K. Optimizing Fuel Economy and Durability of Hybrid Fuel Cell Electric Vehicles Using Deep Reinforcement Learning-Based Energy Management Systems. *Energy Convers. Manag.* **2023**, *291*, 117288. [CrossRef]
8. Lan, S.; Stobart, R.; Chen, R. Performance Comparison of a Thermoelectric Generator Applied in Conventional Vehicles and Extended-Range Electric Vehicles. *Energy Convers. Manag.* **2022**, *266*, 115791. [CrossRef]
9. Peng, J.; He, H.; Xiong, R. Rule Based Energy Management Strategy for a Series–parallel Plug-in Hybrid Electric Bus Optimized by Dynamic Programming. *Appl. Energy* **2017**, *185*, 1633–1643.
10. Liu, Y.; Liu, J.; Zhang, Y.; Wu, Y.; Chen, Z.; Ye, M. Rule Learning Based Energy Management Strategy of Fuel Cell Hybrid Vehicles Considering Multi-Objective Optimization. *Energy* **2020**, *207*, 118212. [CrossRef]

11. Liu, Y.; Wang, M.; Tan, J.; Ye, J.; Liang, J. Real-Time Energy Management Strategy for Fuel Cell Vehicles Based on DP and Rule Extraction. *Energies* **2024**, *17*, 3465. [CrossRef]
12. Shen, Y.; Xie, J.; He, T.; Yao, L.; Xiao, Y. CEEMD-Fuzzy Control Energy Management of Hybrid Energy Storage Systems in Electric Vehicles. *IEEE Trans. Energy Convers.* **2024**, *39*, 555–566.
13. Yadav, S.; Assadian, F. Robust Energy Management of Fuel Cell Hybrid Electric Vehicles Using Fuzzy Logic Integrated with H-Infinity Control. *Energies* **2025**, *18*, 2107. [CrossRef]
14. Tang, X.; Zhou, H.; Wang, F.; Wang, W.; Lin, X. Longevity-conscious Energy Management Strategy of Fuel Cell Hybrid Electric Vehicle Based on Deep Reinforcement Learning. *Energy* **2022**, *238*, 121593. [CrossRef]
15. Hu, X.; Han, J.; Tang, X.; Lin, X. Powertrain Design and Control in Electrified Vehicles: A Critical Review. *IEEE Trans. Transp. Electrif.* **2021**, *7*, 1990–2009. [CrossRef]
16. Zhou, Y.; Ravey, A.; Pera, M.C. Real-time Cost-Minimization Power-Allocating Strategy Via Model Predictive Control for Fuel Cell Hybrid Electric Vehicles. *Energy Convers. Manag.* **2021**, *229*, 113721.
17. Lin, X.; Huang, H.; Xu, X.; Xie, L. Dynamic Programming Solutions Extracted SOC-trajectory Online Learning Generation Algorithm Based Approximate Global Optimization Control Strategy for a Fuel Cell Hybrid Electric Vehicle. *Energy* **2024**, *295*, 130728. [CrossRef]
18. Zhang, L.; Liao, R.; Wei, X.; Huang, W. PMP Method with a Cooperative Optimization Algorithm Considering Speed Planning and Energy Management for Fuel Cell Vehicles. *Int. J. Hydrogen Energy* **2024**, *79*, 434–447. [CrossRef]
19. Guo, N.; Zhang, W.; Li, J.; Chen, Z.; Li, J.; Sun, C. Predictive Energy Management of Fuel Cell Plug-in Hybrid Electric Vehicles: A Co-State Boundaries-Oriented PMP Optimization Approach. *Appl. Energy* **2024**, *362*, 122882.
20. Zhou, S.; Walker, P.; Yang, W.; Nguyen, C.T.; Zhang, N. Energy Management Strategy Design and Fuel Consumption Analysis for a Parallel Hydraulic Hybrid Vehicle. *Int. J. Heavy Veh. Syst.* **2024**, *31*, 187–209. [CrossRef]
21. Tang, X.; Zou, L.; Yang, W.; Huang, Y.; Wang, H. Novel Mathematical Modelling Methods of Comprehensive Mesh Stiffness for Spur and Helical Gears. *Appl. Math. Model.* **2018**, *64*, 524–540. [CrossRef]
22. Tang, X.; Yang, W.; Hu, X.; Zhang, D. A Novel Simplified Model for Torsional Vibration Analysis of a Series-Parallel Hybrid Electric Vehicle. *Mech. Syst. Signal Process.* **2017**, *85*, 329–338. [CrossRef]
23. Liu, Y.; Li, J.; Chen, Z.; Qin, D.; Zhang, Y. Research on a Multi-Objective Hierarchical Prediction Energy Management Strategy for Range Extended Fuel Cell Vehicles. *J. Power Sources* **2019**, *429*, 55–66. [CrossRef]
24. Wang, T.; Li, Q.; Wang, X.; Qiu, Y.; Liu, M.; Meng, X.; Li, J.; Chen, W. An Optimized Energy Management Strategy for Fuel Cell Hybrid Power System Based on Maximum Efficiency Range Identification. *J. Power Sources* **2019**, *445*, 227333.
25. Sporl, K.; Liedtke, R.; Willich, C.; Holzle, M. Model Predictive Energy Management for Fuel Cell Light Commercial Vehicles with State of Health Awareness. *J. Power Sources* **2026**, *666*, 239203.
26. Guo, J.; He, H.; Guo, S. Energy Management Strategy for Fuel Cell Buses Based on Airflow Optimization and Speed Planning. *Int. J. Hydrogen Energy* **2026**, *198*, 152771.
27. Ma, Z.; Zhang, F.; Xie, S.; Zhang, T.; Chen, Y.; Peng, G. Co-optimization of Speed Planning and Energy Management for Connected Plug-in Hybrid Electric Vehicles on Slippery Roads. *Energy* **2025**, *324*, 135835.
28. Yao, Y.; Wang, J.; Zhou, Z.; Li, H.; Liu, H.; Li, T. Hierarchical Predictive Control-Based Economic Energy Management for Fuel Cell Hybrid Construction Vehicles. *Energy* **2023**, *262*, 117327.
29. Su, Q.; Huang, R.; Zhang, Z.; Shou, Y.; He, H. Uncertainty-aware Deep Reinforcement Learning for Trainable Equivalent Consumption Minimization Strategy of Fuel Cell Hybrid Electric Tracked Vehicle. *IEEE Trans. Transp. Electrif.* **2025**, *11*, 10310–10321. [CrossRef]
30. Zhu, Z.; Qiu, X.; Li, C.; Qin, K.; Ji, C.; Jiang, W. Real-time Multi-Objective Energy Management for Fuel Cell Vehicles Via Temporal-Frequency Fusion Speed Prediction and Local Optimal SOC Feedback. *Energy* **2026**, *344*, 139995.
31. Sinu, K.J.; Albert, J.R.; Vanchinathan, K. An Advanced Energy Consumption Predictive Method for Artificial Intelligence-Based Hybrid Electric Vehicle to Improve Vehicle Battery Efficiency for Sustainable Development. *J. Circuits Syst. Comput.* **2025**, *34*, 2650027.
32. Zhou, S.; Ma, Y.; Ming, P.; Li, S.; Yuan, H.; Jiang, B.; Wei, X.; Dai, H. Health-aware Adaptive Energy Management Strategy for Fuel Cell Vehicles Based on Variable Horizon Driving Pattern Recognition. *IEEE Trans. Transp. Electrif.* **2025**, *11*, 11463–11476. [CrossRef]
33. Deng, P.; Wu, X.; Yang, J.; Yang, G.; Jiang, P.; Yang, J.; Bian, X. Optimal Online Energy Management Strategy of a Fuel Cell Hybrid Bus Via Reinforcement Learning. *Energy Convers. Manag.* **2024**, *300*, 117921.
34. Qi, X.; Luo, M.; Zhang, R.; Sui, P.C. Health-aware Energy Management Strategy for Fuel Cell Hybrid Electric Vehicles Based on an Improved Soft Actor-Critic Framework. *Int. J. Hydrogen Energy* **2026**, *205*, 153313.
35. Wu, X.; Ma, P.; Zhou, L.; Fan, Z.; Zhu, Q.; Yin, X.; Ouyang, Q. Collaborative Optimization of Velocity Planning and Energy Management for Fuel Cell Hybrid Buses at Multiple Intersections and Bus Stations. *Energy* **2025**, *326*, 135912. [CrossRef]

36. Shi, D.; Xu, H.; Wang, S.; Hu, J.; Chen, L.; Yin, C. Deep Reinforcement Learning Based Adaptive Energy Management for Plug-in Hybrid Electric Vehicle with Double Deep Q-network. *Energy* **2024**, *305*, 132402. [CrossRef]
37. Dang, H.; Han, Y.; Hao, Y.; Sun, P.; Chen, Z. Energy Management Optimization of Plug-in Hybrid Electric Vehicle in Microgrid with Information-Physics-Traffic Coupling. *Electr. Power Syst. Res.* **2025**, *238*, 111194.
38. Tang, W.; Jiao, X.; Zhang, Y. Hierarchical Energy Management Control for Connected Hybrid Electric Vehicles in Uncertain Traffic Scenarios. *Energy* **2025**, *315*, 134291. [CrossRef]
39. Wang, J.; Liu, K.; Shi, D.; Guo, J.; Wang, Y.; Wang, Y. Adaptive Energy Management Strategy for a Fuel Cell Vehicle Integrated Driving Condition Recognition and Prediction. *Int. J. Green Energy* **2025**, *22*, 2579948.
40. Shi, D.; Li, S.; Xu, H.; Wang, S.; Wang, L. Design and Test of Adaptive Energy Management Strategy for Plug-in Hybrid Electric Vehicle Considering Traffic Information. *Energy* **2025**, *325*, 136093. [CrossRef]
41. Meng, X.; Mei, J.; Tang, X.; Jiang, J.; Sun, C.; Song, K. The Degradation Prediction of Proton Exchange Membrane Fuel Cell Performance Based on a Transformer Model. *Energies* **2024**, *17*, 3050. [CrossRef]
42. Du, J.; Zhang, X.; Wang, S.; Liu, X.; Xing, M. A Novel ANFIS-Dynamic Programming Fusion Strategy for Real-Time Energy Management Optimization in Fuel Cell Electric Commercial Vehicles. *Electronics* **2025**, *14*, 4601.
43. Mei, J.; Meng, X.; Tang, X.; Li, H.; Hasanien, H.; Alharbi, M.; Dong, Z.; Shen, J.; Sun, C.; Fan, F.; et al. An Accurate Parameter Estimation Method of the Voltage Model for Proton Exchange Membrane Fuel Cells. *Energies* **2024**, *17*, 2917. [CrossRef]
44. Ahmed, A.; Ahmad, I. Unit prediction horizon. *Energy* **2024**, *312*, 133445. [CrossRef]
45. Ye, Z.; Ding, Z.; Fu, J.; Xia, G. An MPC-ECMS Integrated Energy Management Strategy for Shipboard Gas Turbine–Photovoltaic–Hybrid Energy Storage Power Systems. *J. Mar. Sci. Eng.* **2026**, *14*, 907.
46. Wang, Y.; Qin, S.; Sun, W.; Bai, S.; Sun, K. Model Predictive Control-Based Energy-Lifetime Co-Optimization Strategy for Commercial Hybrid Electric Vehicles. *Appl. Sci.* **2025**, *15*, 9027.
47. Li, T.; Li, M.; Wang, X.; Cui, J.; Dong, J.; Liu, H.; Xu, H. Adaptive hierarchical energy management strategy for fuel cell hybrid engineering vehicles based on deep reinforcement learning. *Int. J. Hydrogen Energy* **2025**, *168*, 150985. [CrossRef]
48. Ma, B.; Li, P.H. Optimal flexible power allocation energy management strategy for hybrid energy storage system with genetic algorithm based model predictive control. *Energy* **2025**, *324*, 135958. [CrossRef]
49. Du, C.; Gong, K.; Zhang, H.; Zhang, P.; Wu, D.; Liu, X.; Fu, Y. Degradation-considering adaptive equivalent consumption minimization strategy for fuel cell electric vehicles. *Proc. Inst. Mech. Eng. Part D J. Automob. Eng.* **2025**, *239*, 6360–6375.
50. Liu, X.; Du, J.; Ma, J.; Liu, G.; Xiong, Y. An Adaptive Co-State Design Method for Pmp-Based Energy Management of Plug-In Hybrid Electric Vehicles Based on Fuzzy Logical Control. *J. Energy Storage* **2024**, *102*, 114118.
51. Meng, X.; Liu, M.; Mei, J.; Li, X.; Grigoriev, S.; Hasanien, H.M.; Tang, X.; Li, R.; Sun, C. Polarization loss decomposition-based online health state estimation for proton exchange membrane fuel cells. *Int. J. Hydrogen Energy* **2025**, *157*, 150162. [CrossRef]
52. Tang, X.; Yang, M.; Shi, L.; Hou, Z.; Xu, S.; Sun, C. Adaptive state-of-health temperature sensitivity characteristics for durability improvement of PEM fuel cells. *Chem. Eng. J.* **2024**, *491*, 151951. [CrossRef]
53. Meng, X.; Sun, C.; Mei, J.; Tang, X.; Hasanien, H.M.; Jiang, J.; Fan, F.; Song, K. Fuel Cell Life Prediction Considering the Recovery Phenomenon of Reversible Voltage Loss. *J. Power Sources* **2025**, *625*, 235634. [CrossRef]

**Disclaimer/Publisher's Note:** The statements, opinions and data contained in all publications are solely those of the individual author(s) and contributor(s) and not of MDPI and/or the editor(s). MDPI and/or the editor(s) disclaim responsibility for any injury to people or property resulting from any ideas, methods, instructions or products referred to in the content.